Monthly Notices
of the
ROYAL ASTRONOMICAL SOCIETY

MNRAS **467,** 4322–4342 (2017)
Advance Access publication 2017 February 9

doi:10.1093/mnras/stx341

The turbulent life of dust grains in the supernova-driven, multiphase interstellar medium

Thomas Peters,[1]★ Svitlana Zhukovska,[1] Thorsten Naab,[1] Philipp Girichidis,[1] Stefanie Walch,[2] Simon C. O. Glover,[3] Ralf S. Klessen,[3,4] Paul C. Clark[5] and Daniel Seifried[2]

[1]*Max-Planck-Institut für Astrophysik, Karl-Schwarzschild-Str. 1, D-85748 Garching, Germany*
[2]*I. Physikalisches Institut, Universität zu Köln, Zülpicher Strasse 77, D-50937 Köln, Germany*
[3]*Zentrum für Astronomie, Institut für Theoretische Astrophysik, Universität Heidelberg, Albert-Ueberle-Str. 2, D-69120 Heidelberg, Germany*
[4]*Interdisziplinäres Zentrum für Wissenschaftliches Rechnen (IWR), Universität Heidelberg, D-69120 Heidelberg, Germany*
[5]*School of Physics and Astronomy, Cardiff University, 5 The Parade, Cardiff CF24 3AA, Wales, UK*

Accepted 2017 February 7. Received 2017 February 3; in original form 2016 September 6

ABSTRACT

Dust grains are an important component of the interstellar medium (ISM) of galaxies. We present the first direct measurement of the residence times of interstellar dust in the different ISM phases, and of the transition rates between these phases, in realistic hydrodynamical simulations of the multiphase ISM. Our simulations include a time-dependent chemical network that follows the abundances of H^+, H, H_2, C^+ and CO and take into account self-shielding by gas and dust using a tree-based radiation transfer method. Supernova explosions are injected either at random locations, at density peaks, or as a mixture of the two. For each simulation, we investigate how matter circulates between the ISM phases and find more sizeable transitions than considered in simple mass exchange schemes in the literature. The derived residence times in the ISM phases are characterized by broad distributions, in particular for the molecular, warm and hot medium. The most realistic simulations with random and mixed driving have median residence times in the molecular, cold, warm and hot phase around 17, 7, 44 and 1 Myr, respectively. The transition rates measured in the random driving run are in good agreement with observations of Ti gas-phase depletion in the warm and cold phases in a simple depletion model. ISM phase definitions based on chemical abundance rather than temperature cuts are physically more meaningful, but lead to significantly different transition rates and residence times because there is no direct correspondence between the two definitions.

Key words: methods: numerical – ISM: clouds – dust, extinction – ISM: evolution – galaxies: ISM – galaxies: star formation.

1 INTRODUCTION

Refractory sub-μm particles or dust grains are an integral component of the interstellar medium (ISM) of galaxies. Interstellar dust consists of silicate and carbonaceous grains with a mass fraction of less than 1 per cent of the gas mass. Nevertheless, these dust grains influence the physics and chemistry of the ISM in multiple ways (Tielens 2010; Draine 2011). One of the most important effects of interstellar grains is their absorption of the ultraviolet (UV) interstellar radiation field. At least 30 per cent of the stellar light at UV wavelengths is reprocessed by grains and re-emitted in the infrared (Soifer et al. 1987). A small fraction of the absorbed energy is returned to the ISM through photoelectric emission, which is the dominant heating source of the diffuse ISM (Bakes & Tielens 1994). Dust also affects the thermal balance of the ISM by locking away important coolants such as C^+ and Si^+ (Bekki 2015; McKinnon, Torrey & Vogelsberger 2016) and by causing the freeze-out of CO in the dense phase (Goldsmith 2001; Bergin & Tafalla 2007; Hollenbach et al. 2009; Caselli 2011; Fontani et al. 2012; Hocuk, Cazaux & Spaans 2014). Grains have a two-fold role in astrochemistry, namely shielding the molecules from the dissociating UV photons and providing the surfaces for the formation of complex organic molecules and H_2 molecules, the main constituent of molecular clouds. The size distribution and chemical composition are the key dust properties determining grain interactions with matter and radiation.

Numerical simulations of galactic evolution usually assume that interstellar dust constitutes a fixed fraction of the metals and that its properties have the average characteristics of dust in the local

★ E-mail: tpeters@MPA-Garching.MPG.DE

Galaxy (Walch et al. 2015, and references therein). However, there is strong observational evidence that grain properties depend on the local environment, as indicated by large sightline-to-sightline variations of extinction curves (Fitzpatrick & Massa 2007) and interstellar element depletion (Jenkins 2009). It has been demonstrated that dust opacities at submillimetre wavelengths change from the diffuse to the dense ISM (Martin et al. 2012; Roy et al. 2013; Planck Collaboration XI 2014). Variations in the ratio of dust opacities at far-infrared and visible/UV wavelengths found in the diffuse ISM imply that dust properties differ not only between the ISM phases, but also on small scales within the diffuse H I gas (Planck Collaboration XXIV 2011; Planck Collaboration XVII 2014).

The observed changes in dust properties are attributed to grain evolution driven by local conditions in the ISM. In a simplified way, the ISM can be described by a three-phase model proposed by McKee & Ostriker (1977), which consists of cold clouds (cold neutral medium, CNM), surrounded by the warm neutral envelopes (warm neutral medium, WNM) and warm ionized matter (WIM); the hot ionized medium fills most of the volume. Additionally, molecular clouds represent dense regions of the ISM that are opaque to UV radiation and where star formation takes place. Due to their coupling to the interstellar gas, interstellar grains follow the cycle of matter between the ISM phases, which is regulated by the formation of molecular clouds and their disruption by stellar feedback processes (e.g. Wooden, Charnley & Ehrenfreund 2004; Dobbs, Pringle & Burkert 2012).

During their time in the warm medium, grains are altered and partially or completely destroyed by a number of processes such as vaporization in grain–grain collisions and erosion by ion sputtering in interstellar shocks, and by UV irradiation by the interstellar radiation field (McKee 1989; Jones et al. 1994; Tielens et al. 1994; Jones, Tielens & Hollenbach 1996; Jones et al. 2013; Slavin, Dwek & Jones 2015). In clouds, grains are protected from UV irradiation and sputtering in shocks, and the dust mass can grow by accretion of gas-phase species (Greenberg 1982; Draine 2009). Coagulation becomes the dominant outcome of grain–grain collisions in dense clouds, resulting in the removal of small grains and the build-up of large grains (Hirashita & Yan 2009; Ormel et al. 2011).

Dust abundances in the interstellar gas are therefore closely related to the evolution of the ISM, in particular to its structure and the mass transfer between the phases. To explain the large differences in element depletion between the WNM and CNM (Savage & Sembach 1996), simple models of dust evolution based on two- and three-phase ISM models with various schemes for phase transitions were proposed in the literature (Draine 1990; O'Donnell & Mathis 1997; Tielens 1998; Weingartner & Draine 1999). Draine (1990) demonstrated that the relative depletion in the CNM and WNM depends on the adopted scheme of the phase transition: whether gas from the WNM is transferred directly to molecular clouds or through the CNM. Moreover, the observed scatter in the dust-to-gas ratio in spiral galaxies can also be explained by the cycling of matter in the multiphase ISM, with the time-scales of the transitions determining the amplitude of the dust-to-gas ratio variations (Hirashita 2000).

The residence times that the grains spend in the different ISM phases are important quantities that regulate the processing of the grains in these environments. Hirashita & Yan (2009) demonstrated that the grain size distribution is very sensitive to the residence times in the ISM phases: grain shattering by turbulence can overproduce the number of small grains in the WIM and limit the sizes of large grains in the WNM. Coagulation dominating in dense cloud cores can completely remove small grains when the residence time exceeds 10 Myr.

The residence times in the multiphase ISM also determine the exposure of interstellar grains to UV radiation and the susceptibility to collisions with ions. Information on the exposure duration is useful to set up realistic conditions for laboratory experiments on dust analogues simulating the formation and evolution of organic refractory matter (Jenniskens et al. 1993). Moreover, some stardust grains present in the Solar system during its formation process can be identified in meteorites and studied in the laboratory. Analysis of the surfaces of these grains provides insights into their processing in the ISM and can be done more accurately if the exposure times are known (Gyngard et al. 2009; Heck et al. 2009; Amari, Zinner & Gallino 2014).

Models of interstellar dust typically use a highly idealized description of the ISM phases, where each phase is represented by a single characteristic temperature and density. Recent, more realistic hydrodynamical simulations of the ISM (Walch et al. 2015; Girichidis et al. 2016a) present an opportunity to move away from this simplified picture. They allow us to probe dust evolution in the context of an inhomogeneous ISM under a wide range of physical conditions and a complex evolutionary history. For example, in such simulations molecular clouds form dynamically out of the diffuse phase and get destroyed by stellar feedback. The physical conditions within the molecular cloud are then time-dependent, and there will be a distribution of molecular cloud lifetimes rather than a single unique value.

In this paper, we investigate the lifecycle of interstellar grains in the multiphase ISM with simulations from the SImulating the LifeCycle of molecular Clouds (SILCC) project (Walch et al. 2015; Girichidis et al. 2016a). The SILCC simulations include a time-dependent chemical network and therefore provide detailed descriptions of the relevant ISM structure and phases. We present a pilot study in which we use Lagrangian tracer particles to measure residence times in and transition rates between the different ISM phases in local galactic-scale simulations of a supernova-driven ISM under solar neighbourhood conditions. Details of our numerical scheme and the simulation setup are given in Section 2. We describe the evolution of the simulations in Section 3 and of individual tracer particle trajectories in Section 4. We then discuss how the tracer particles sample the multiphase ISM (Section 5) and present our measurements of mass circulation and transition rates between the phases (Section 6), residence times within the phases (Section 7) and shielding from UV radiation (Section 8). We point out some caveats in Section 9 and conclude in Section 10.

2 SIMULATIONS

We present kpc-scale stratified box simulations run with the adaptive mesh refinement code FLASH 4 (Fryxell et al. 2000; Dubey et al. 2009) with a stable, positivity-preserving magnetohydrodynamics solver (Bouchut, Klingenberg & Waagan 2007; Waagan 2009; Waagan, Federrath & Klingenberg 2011) and a method based on a Barnes–Hut tree (Barnes & Hut 1986) to incorporate self-gravity (R. Wünsch et al. in preparation). Our simulation box has dimensions $0.5\,\mathrm{kpc} \times 0.5\,\mathrm{kpc} \times 2.5\,\mathrm{kpc}$ and a maximum grid resolution of 3.9 pc. We apply periodic boundary conditions in the plane of the disc (x and y directions) and outflow boundary conditions in the vertical (z) direction, so that gas can leave but not enter the simulation box. The simulation domain has lower heights above and below the disc plane than previous SILCC simulations (Walch

et al. 2015; Girichidis et al. 2016a), but otherwise the code and setup are identical.

We impose an external potential to model the gravitational force of a stellar disc on the gas. We choose an isothermal sheet potential with parameters that fit solar neighbourhood values, namely a stellar surface density $\Sigma_* = 30\,\mathrm{M}_\odot\,\mathrm{pc}^{-2}$ and a vertical scaleheight $z_\mathrm{d} = 100\,\mathrm{pc}$. We set up the gas with a Gaussian distribution in z direction, with a scaleheight of 60 pc, and a gas surface density $\Sigma_\mathrm{gas} = 10\,\mathrm{M}_\odot\,\mathrm{pc}^{-2}$. The simulations presented in this paper do not include magnetic fields. For more information on the initial conditions and simulation setup see Walch et al. (2015) and Girichidis et al. (2016a).

We use a time-dependent chemical network (Nelson & Langer 1997; Glover & Mac Low 2007a,b; Glover & Clark 2012) that follows the abundances of free electrons, H^+, H, H_2, C^+, O and CO. We employ the `TreeCol` algorithm (Clark, Glover & Klessen 2012, R. Wünsch et al. in preparation) to take into account dust shielding and molecular self-shielding. In the warm and cold gas, the primary cooling processes are Lyman α cooling, H_2 ro-vibrational line cooling, fine-structure emission from C^+ and O and rotational emission from CO (Glover et al. 2010; Glover & Clark 2012). In hot gas, electronic excitation of helium and of partially ionized metals must also be taken into account, which is done using the Gnat & Ferland (2012) cooling rates assuming collisional ionization equilibrium. Furthermore, we include diffuse heating from the photoelectric effect, cosmic rays and X-rays following the prescriptions of Bakes & Tielens (1994), Goldsmith & Langer (1978) and Wolfire et al. (1995), respectively. More information on the chemical network and the various heating and cooling processes can be found in Gatto et al. (2015) and Walch et al. (2015).

For our gas surface density, the Kennicutt–Schmidt relation (Schmidt 1959; Kennicutt 1998) yields a star formation rate surface density $\Sigma_\mathrm{SFR} = 6 \times 10^{-3}\,\mathrm{M}_\odot\,\mathrm{yr}^{-1}\,\mathrm{kpc}^{-2}$. Assuming one supernova event per $100\,\mathrm{M}_\odot$ in stars, this corresponds to a supernova rate surface density $\Sigma_\mathrm{SN} = 60\,\mathrm{Myr}^{-1}\,\mathrm{kpc}^{-2}$, or 15 supernova explosions per Myr in our simulation volume. We inject a thermal energy $E_\mathrm{SN} = 10^{51}$ erg with each such explosion at this constant rate.

We consider three different ways to position the sites of the supernova explosions (see Girichidis et al. 2016a for a detailed justification). For random driving, we distribute the explosion sites according to a probability distribution that is uniform in the x–y plane and Gaussian in z direction with a scaleheight of 50 pc (Tammann, Löffler & Schröder 1994). For peak driving, supernovae always explode at the current location of the maximum density peak. For mixed driving, 50 per cent of all supernovae are randomly distributed and 50 per cent explode at density peaks. We refer to Gatto et al. (2015) for details on the implementation of supernova positioning and energy injection and to Walch et al. (2015) and Girichidis et al. (2016a) for a systematic investigation of the effects of supernova positioning and supernova rates on the chemical and dynamical properties of the resulting ISM, respectively. In their notation, our simulations with random, mixed and peak driving correspond to the runs S10-KS-rand, S10-KS-mix and S10-KS-peak, respectively. We have run all three simulations for a duration of 80 Myr.

Our simulations represent an idealization of star formation feedback in the ISM. Because we do not model the formation of star clusters self-consistently (but see Gatto et al. 2017; Peters et al. 2017), we systematically explore how the location of supernova explosions affects the ISM. Peak driving is motivated by the idea that star formation happens in the densest regions of the ISM. Random driving takes the finite time between the formation of stars and their explosions as supernovae as well as the existence of field and runaway OB stars into account, which leads to the expectation that a large fraction of supernovae are located in underdense gas at random positions. Mixed driving is a compromise between the two extremes. The ISM is most realistic for simulations with random and mixed driving in terms of mass fractions and volume-filling fractions of the different ISM phases, while with peak driving the formation of H_2 and the hot phase is suppressed (Walch et al. 2015). Although some dynamical quantities like velocity dispersions and outflow rates converge, the simulations do not reach a steady state because they do not include a self-consistent treatment of star formation and supernova explosions (Girichidis et al. 2016a). They should be understood as controlled numerical experiments that allow us to study the properties of interstellar dust in the multiphase ISM produced by the different forms of supernova driving.

At the beginning of each simulation, we distribute $N_\mathrm{part} = 10^6$ tracer particles over the simulation volume such that the local tracer particle number density is proportional to the local gas density. The equation of motion for the tracer particles is integrated using Heun's method, which is a second-order, two-stage Runge–Kutta scheme. The tracer particle equations of motion are integrated via

$$\boldsymbol{r}^*(t_{i+1}) = \boldsymbol{r}(t_i) + \Delta t_i \times \boldsymbol{u}(\boldsymbol{r}(t_i), t_i), \tag{1}$$

$$\boldsymbol{r}(t_{i+1}) = \boldsymbol{r}(t_i) + \frac{\Delta t_i}{2} \times \Big(\boldsymbol{u}(\boldsymbol{r}(t_i), t_i) + \boldsymbol{u}(\boldsymbol{r}^*(t_{i+1}), t_{i+1})\Big), \tag{2}$$

$$\boldsymbol{v}(t_{i+1}) = \boldsymbol{u}(\boldsymbol{r}(t_{i+1}), t_{i+1}). \tag{3}$$

Here, t_i is the current simulation time, Δt_i is the current timestep and $t_{i+1} = t_i + \Delta t_i$. The tracer particle position vector is denoted as $\boldsymbol{r}$ and its velocity vector as $\boldsymbol{v}$. The gas velocity vector field $\boldsymbol{u}$ is tri-linearly interpolated from the grid to the particle location. The quantity $\boldsymbol{r}^*$ is a predictor-type variable and only of temporary use. We interpolate the data stored on the grid (gas density and temperature, chemical abundances and the local radiation field) to the location of the particle within the grid tri-linearly and save it together with the particle positions and velocities to a file every 10 kyr, which is a factor of a few larger than the typical simulation timestep. The tracer particles are passive and do not affect the dust abundance used in the chemical network, which we assume to be constant. Furthermore, we do not inject any additional particles during the simulation since the time-scale of dust production is long compared to the total runtime.

The tracer particles are interpreted as representative ensembles of dust grains. We can assign a mass to each tracer particle by assuming that the total mass of dust is equally distributed among all tracer particles. For simplicity, we adopt the constant gas-to-dust mass ratio of 162 derived for the interstellar dust model BARE-GR-S, which consists of bare silicate and graphitic grains (Zubko, Dwek & Arendt 2004). A higher gas-to-dust ratio than a commonly used value of 100 is required by interstellar dust models that simultaneously fit dust extinction, infrared diffuse emission and element abundance constraints (Zubko et al. 2004; Draine & Li 2007). For a gas-to-dust ratio of 162 and a total gas mass in the simulation volume $M_\mathrm{gas} = 2.5 \times 10^6\,\mathrm{M}_\odot$, the tracer particle mass becomes

$$m_\mathrm{part} = \frac{M_\mathrm{gas}}{162\,N_\mathrm{part}} = 1.5 \times 10^{-2}\,\mathrm{M}_\odot. \tag{4}$$

This definition allows us to convert between tracer particle numbers and dust masses.

The BARE-GR-S dust model is designed to match various observational constraints in the local diffuse ISM. It is known that the

gas-to-dust ratio in the dense gas can be a few times lower compared to the diffuse ISM owing to accretion of gas-phase species on to grain surfaces. It is however very difficult to infer the true variations of the gas-to-dust ratio from observed dust emission maps, because it requires one to disentangle the effects of a number of different physical processes that affect dust emission in translucent molecular clouds: changes of the far-infrared dust properties due to coagulation of grains, the contribution of the CO-dark molecular gas to the gas-to-dust ratio and the true decrease in the gas-to-dust ratio due to the dust growth in the ISM (Roman-Duval et al. 2014). Recent models of dust evolution in the inhomogeneous multiphase ISM study the variations of silicate dust abundance with local conditions, but are still uncertain in variations in the gas-to-dust ratio (Zhukovska et al. 2016).

The difference in element depletion between the lines of sight with the lowest and the highest depletion levels in the large sample of data compiled by Jenkins (2009) implies a variation of the gas-to-dust ratio of a factor of 2. With this factor, the dust mass associated with a tracer particle $m_{\rm part}$ in the dense phase can be higher, which is presently neglected in this work.

3 DISTRIBUTION OF TRACER PARTICLES

The gas flow in the simulations is created mainly by two dynamical processes: gravity, which pulls the gas towards the disc mid-plane and leads to the formation of self-gravitating molecular clouds, and blast waves that are created by supernova explosions. As the gas moves, the tracer particles are advected with the flow. In a compressible gas, the number density of tracer particles is roughly proportional to the gas density. Therefore, tracer particles tend to accumulate in dense regions, and only relatively few tracer particles are present in voids or get injected into the halo. A very small fraction of tracer particles leaves the simulation box at $z = \pm 1.25$ kpc during the simulation runtime: 2.95 per cent for random driving, 0.04 per cent for mixed driving and 0.02 per cent for peak driving. Since we do not know the fate of these particles, we only include tracer particles in our subsequent analysis that stay within the simulation box until the end.

Fig. 1 shows face-on and edge-on gas column densities together with the tracer particle locations for random, mixed and peak driving after 40 Myr of evolution.[1] At the start of the simulation, the gas collapses towards the disc mid-plane until the supernova explosions have created enough thermal and kinetic pressure to support the gas against collapse. After 10 Myr, the random supernova driving has left a large fraction of the initial particle distribution in the disc plane unaffected, whereas the tracer particles are completely mixed after 40 Myr. As the simulations proceed, self-gravitating structures form that resist destruction by supernova blast waves. At 80 Myr, most of the tracer particles reside in a few dense regions and within an outflow driven by supernova explosions from the diffuse medium.

For the case of mixed driving, some differences occur. Here, every second explosion is located at density peaks. Injecting supernovae at the places of highest density can lead to a runaway process when the supernova injection triggers the formation of a blast wave that creates a high-density shock. The density peak at the moment of the next supernova injection will then likely be located somewhere at the density enhancement created by this shock. A repeated injection of supernovae in a relatively small volume can then lead to an amplification of density contrasts that attracts subsequent supernova injections. This is what happens here in the first 10 Myr and what creates the spherical region visible in the face-on projection. Because only half of all supernovae explode at random positions, a large fraction of the particles remain unperturbed by supernova explosions at this time. However, after 40 Myr also in this simulation the tracer particles are completely mixed, and the disc scaleheight is similar to the simulation with random driving. Once the ISM has a sufficiently complex structure, the influence of the density peak supernovae on the mixing is reduced because a certain region in the disc is no longer favoured for supernova injections. The final snapshot at 80 Myr also looks similar to the situation for random driving.

In the simulation with pure peak driving, the evolution is markedly different. Now, all supernovae explode within a region of diameter ~ 0.2 kpc in the first 10 Myr because of the described runaway process. Supernova explosion sites propagate radially outwards from the location of the first explosion. At 40 Myr, the ISM has a complex structure and the tracer particles are fully mixed. However, the initially clustered supernova explosions have created a cavity that remains for the rest of the simulation runtime. Since supernovae are injected at density peaks, much less hot gas is created, and almost no galactic wind is driven (Girichidis et al. 2016a). At 80 Myr, the gas density in the disc is higher than for random and mixed driving, and the tracer particles are more homogeneously distributed.

4 INDIVIDUAL TRAJECTORIES

While ISM dust models typically represent the ISM phases with a single characteristic temperature, a more accurate phase definition assigns a whole temperature range to each phase (e.g. Ferrière 2001). Guided by our previous study of ISM phases in the SILCC simulations by Walch et al. (2015), we consider four different phases defined by temperature cuts in this paper:

(i) molecular phase ($T < 50$ K),
(ii) cold phase ($50 \leq T < 300$ K),
(iii) warm phase ($300 \leq T < 3 \times 10^5$ K),
(iv) hot phase ($T \geq 3 \times 10^5$ K).

There are two important differences to our analysis in Walch et al. (2015). First, we do not include a warm-hot phase because it is thermally unstable and therefore short-lived. Hence, we subsume the warm-hot phase from Walch et al. (2015) in our warm phase. Secondly, we choose a slightly higher temperature cut of 50 K to separate the molecular and the cold phase instead of 30 K as in Walch et al. (2015).

The reason for this higher temperature cut becomes evident from Fig. 2, where we plot the temperature histories of 10 randomly selected particles from the simulation with random driving. At our spatial grid resolution of 3.9 pc, we barely resolve temperatures below 30 K, so that this threshold value would lead to artificially low residence times in the molecular phase and artificially high transition rates between the molecular and the cold phase.

In Walch et al. (2015), we compared our simulation results with the classical McKee & Ostriker (1977) pressure equilibrium model of a three-phase ISM. We found that the hot gas pressure in our simulations is in approximate equilibrium with the warm phase, and that the volume-filling fraction of the hot gas, which fills

[1] An animated version of this figure can be found on the SILCC project website http://hera.ph1.uni-koeln.de/~silcc/.

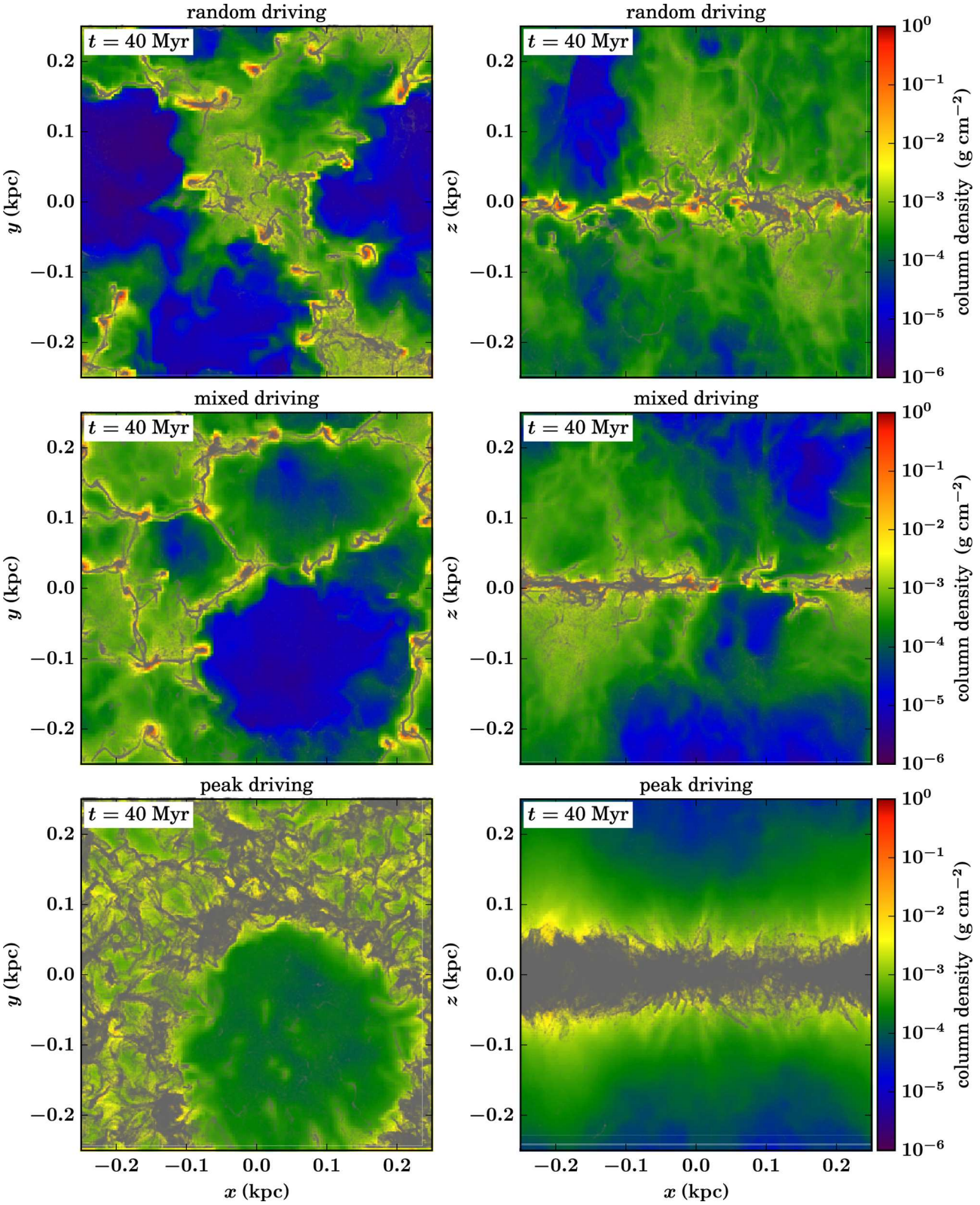

Figure 1. Projections of gas density (left: face-on, right: edge-on) for the simulation with random driving (top), mixed driving (middle) and peak driving (bottom) after 40 Myr of evolution. In the z-direction, only the inner 0.25 kpc of the whole box height (1.25 kpc) is shown. Each tracer particle is represented by a grey dot. Movies of the simulations are available on the SILCC website.

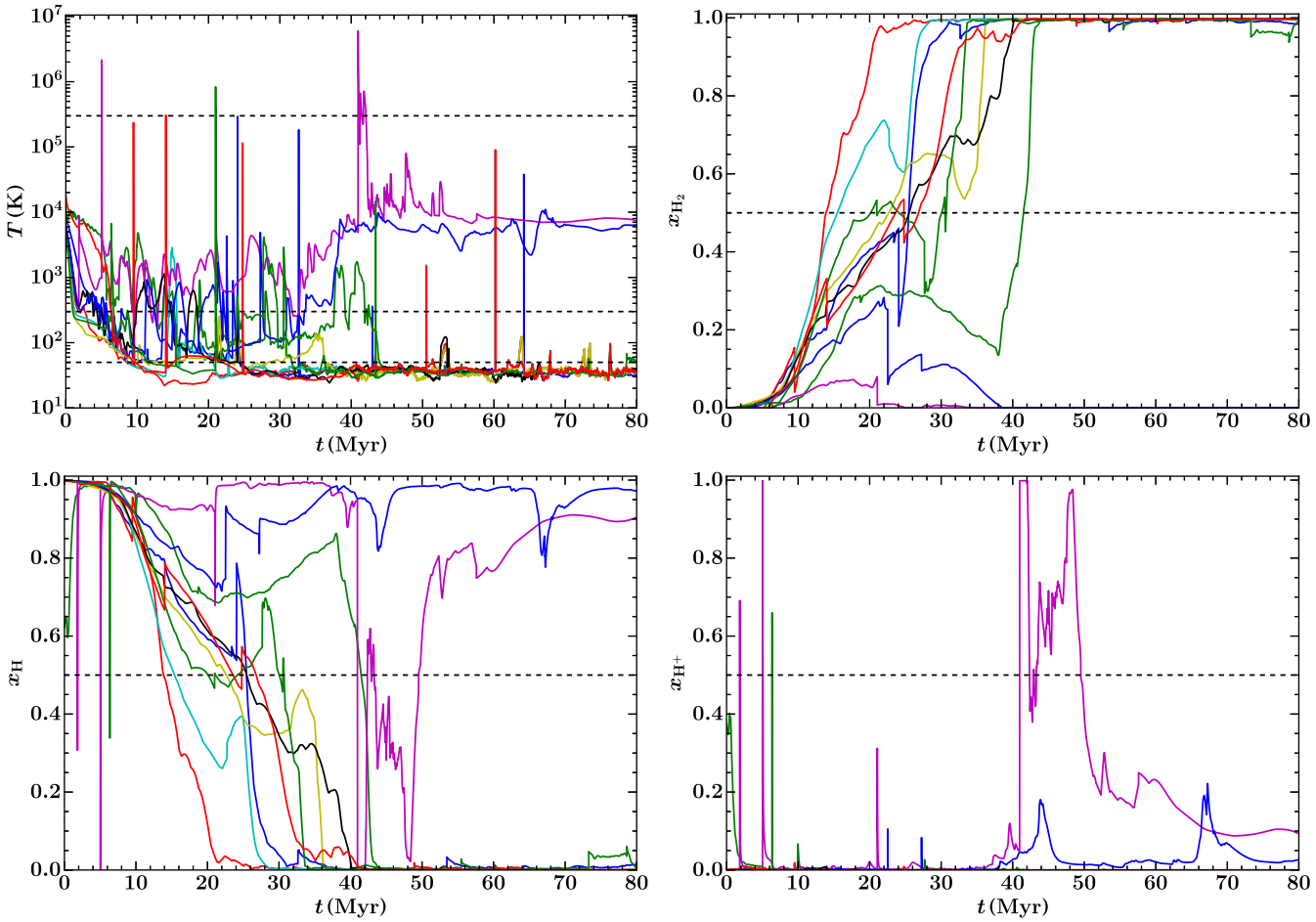

Figure 2. Histories of temperature and molecular, atomic and ionized hydrogen mass fractions for 10 randomly selected particles from the simulation with random driving. The dashed lines indicate the phase boundaries. The individual particles are identically coloured in the four panels. The particles have complex evolutionary histories and typically change their ISM phase multiple times during the simulation.

the intercloud volume, is in agreement with predictions of this model.

We stress that Walch et al. (2015) have shown that the temperature cuts do not directly correspond to transitions in the chemical composition. We therefore define a second, independent, set of ISM phases using the chemical abundances of the different forms of hydrogen in our chemical network, or more precisely their corresponding mass fractions x:

(i) H_2 phase ($x_{H_2} > 50$ per cent),
(ii) H phase ($x_H > 50$ per cent),
(iii) H^+ phase ($x_{H^+} > 50$ per cent).

The histories of the mass fractions are also shown in Fig. 2 for the same 10 particles. The time evolution of the chemical abundances is much smoother than the temperature evolution. In part, this is because the chemical time-scale is often much longer than the dynamical time-scale or cooling time-scale, meaning that the chemical makeup of the gas frequently lags behind its thermal state. Consequently, if the duration of a heating event and the subsequent cooling is short enough, the gas can move from one thermal phase to another and back again without ever significantly changing its chemical state. In addition, the temperature cuts that we use to define our different thermal phases are often only weakly correlated with chemical changes in the gas. For example, although the temperature range we adopt for our 'molecular' phase is a relatively good match for the temperature inferred from CO observations, there is both observational and theoretical evidence that CO-dark H_2 occupies a much broader range of temperatures (Rachford et al. 2009; Glover & Smith 2016). Therefore, gas moving from the CO-bright regime to the CO-dark regime will undergo a transition from our 'molecular' to our 'cold' phase, but may remain dominated by H_2 throughout.

Since there is no one-to-one correspondence between the two sets of phase definitions (see also discussion in Walch et al. 2015), the chemical abundance cuts provide a separate set of statistics for residence times and transition rates. These data are more physically meaningful but harder to compare to values in the literature because they are different from the traditional ISM phase definitions.

The displayed evolutionary tracks illustrate the complexity of interpreting the data in terms of grain properties. For example, in gas that is dense enough to shield itself from the interstellar radiation field, allowing molecular hydrogen to form, ice mantles can grow on the surfaces of dust grains. However, the tracks demonstrate that particles in the H_2 phase are not protected from high temperatures, and even short periods of heating beyond the evaporation temperature (or exposure to UV radiation) can destroy the ice mantles again. We conclude that a single physical quantity (density, column density, temperature or chemical composition) is not enough to

characterize the grain properties, but all of them must be considered in concert.

5 SAMPLING OF THE MULTIPHASE ISM

As the tracer particles get advected with the flow, they sample the entire phase space of the multiphase ISM. Initially, they are homogeneously distributed across the disc, with a tracer particle number density that scales with the gas density. When the gas starts to move, regions of compressed gas will contain more tracer particles than voids. Naturally, since the molecular and cold phase have a higher gas density than the warm and hot phase, the number density of tracer particles residing in these phases will also be larger. Because the density contrast in the ISM amounts to several orders of magnitude, we may inadequately sample the underdense gas with our $N_{\rm part} = 10^6$ tracer particles.

To check how well the fraction of particles $f_{\rm part}$ in the different ISM phases represents the corresponding total gas mass fractions X, we plot both quantities for the three simulations as a function of time t in Fig. 3 for the ISM phases defined by temperature cuts and in Fig. 4 for the chemical abundance cuts. We see that for random and mixed driving, we need about 10 Myr to produce a molecular phase with a total mass fraction in excess of 10 per cent. After this time, the mass fractions of the four phases only change within a factor of a few.

However, the particle fractions evolve notably differently than the mass fractions. The particle fraction in the molecular phase steadily increases over the simulation time, while the particle fraction in the cold phase decreases. A growing number of particles fall into the deep gravitational potential wells of molecular clouds (compare Fig. 1) and enter the molecular phase from the cold phase, explaining these overall trends. They can only escape from these regions when a supernova explodes in a nearby location. During such an event, a large number of particles get ejected instantaneously from the molecular into the cold phase, from where they fall back into the molecular phase by gravitational attraction. This is the reason for the series of spikes that are superimposed on the general trend for the cold phase evolution after 40 Myr. The particle fractions of the warm and hot phase remain roughly constant, although the hot phase shows large fluctuations due to the small absolute particle numbers in this phase.

For peak driving, the situation is qualitatively different. Here, continuous supernova explosions in the dense gas delay the formation of a molecular phase substantially. It takes 60 Myr until the mass fraction for the molecular phase reaches similar values as for random and mixed driving. Simultaneously, the hot phase disappears completely. The regions in which the supernovae explode are now so dense that no significant amount of hot gas is produced anymore.

In general, the particle fractions $f_{\rm part}$ and the total gas mass fractions X agree within a factor of a few. In absolute values, the differences are largest in the molecular phase, while the biggest relative error between $f_{\rm part}$ and X occurs for the hot phase. Because of the discrepancies between $f_{\rm part}$ and X, we must be aware that the tracer particles do not equally sample the full simulation box. We note that this may be due to a fundamental problem of Lagrangian tracer particles in highly compressible flows (Genel et al. 2013), and therefore the mismatch is unlikely to be solved by simply increasing the total number of tracer particles. Instead, early stellar feedback from winds (Gatto et al. 2017) and radiation (Peters et al. 2017) may prevent the tracer particles from being locked inside clouds and facilitate a much better circulation of the particles through the different ISM phases. If early feedback does not alleviate the problem, an implementation of Monte Carlo tracer particles following Genel et al. (2013) will be necessary to accurately follow the mass flux between the ISM phases. Because of the discrepancies between $f_{\rm part}$ and X with our current tracer particle implementation, we introduce systematic errors in our measured residence times and transition rates. For example, since we overestimate the molecular phase mass fraction, we also overestimate the residence times in the molecular phase. This may be because the transition rates into the molecular phase are too high, the transition rates out of the molecular phase are too low, or both. A quantitative evaluation of this error is very difficult without an improved numerical method.

The evolution of the chemical phases shown in Fig. 4 is more regular compared to the temperature cuts, which can be directly traced back to the less erratic individual trajectories. The definition of the chemical phases is more robust with respect to perturbations. In particular, supernova explosions near molecular clouds do not eject a large number of locked particles into regions where the molecular mass fraction is less than 50 per cent, so that these particles do not change their phase. In general, the agreement between particle fractions and total gas mass fractions is better than for the temperature cuts. A substantial difference in the time evolution of the ISM phases between the simulations can be observed in the run with peak driving, where an H_2 phase is beginning to build up at 20 Myr but then gets completely destroyed again at 40 Myr. The H_2 phase can only persist after 60 Myr. In this simulation, the H phase is by far dominant for most of the simulation runtime because the supernova explosions at density peaks can very effectively delay the formation of significant amounts of molecular hydrogen.

6 TRANSITION RATES

Mass exchange between the ISM phases plays an important role in the lifecycle of interstellar grains. It controls the circulation of gas from the WNM, where dust abundances are reduced by destruction in interstellar shocks, and matter enriched with dust due to accretion on grain surfaces at higher gas densities. Several models of dust evolution in the idealized two- and three-phase ISM have been proposed to explain the observed differences between element depletion in the warm medium and cold clouds (Draine 1990; O'Donnell & Mathis 1997; Tielens 1998; Weingartner & Draine 1999). Models with a two-phase ISM neglect the difference between the molecular and diffuse H I clouds and consider mass circulation only between the ambient warm medium and clouds (O'Donnell & Mathis 1997; Tielens 1998). O'Donnell & Mathis (1997) showed that a three-phase ISM model with an additional mass exchange with the molecular clouds reproduces the observations better. Assuming a steady state for the interchange between phases and time-scales of dust destruction and accretion, one can estimate the rates of mass exchange required to reproduce the observed element depletion (Draine 1990; Weingartner & Draine 1999). The resulting rates, however, depend on the adopted scheme of mass transfer between phases that in the case of the three-phase ISM can occur via different routes. For example, depending on whether the WNM is converted to molecular clouds directly or through the CNM, the mass exchange rates between the CNM and molecular clouds can differ by a factor of 8 (Draine 1990).

In addition to the mass circulation scheme, the outcome of dust evolution models depends on the implementation of dust destruction by supernova shocks and dust growth by accretion in clouds, which introduce more uncertainties in the models. For example, unknown details of the growth process, in particular, the efficiency of sticking

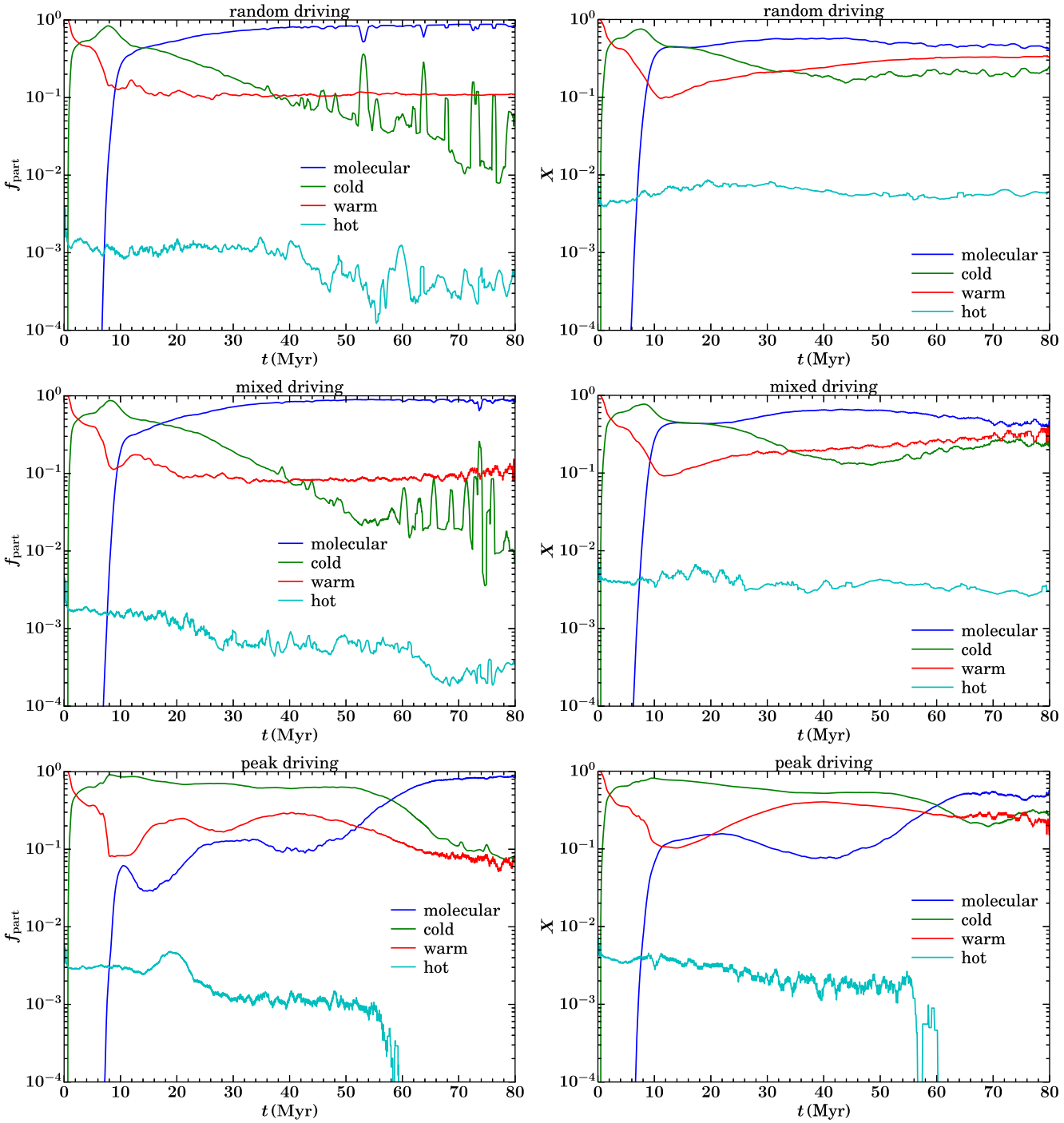

Figure 3. Particle fractions $f_{\rm part}$ (left) and total gas mass fractions X (right) for the different ISM phases defined by temperature cuts as function of time t for random (top), mixed (middle) and peak (bottom) driving.

of incident species on the grain surfaces can strongly affect the value of the accretion time-scale and the resulting dust abundance distribution (Zhukovska et al. 2016).

In this work, we clarify the uncertainties in dust evolution modelling with respect to the matter cycle and mass exchange scheme by means of numerical simulations of the turbulent ISM and provide a basis for studies of grain processing in the ISM. The simulations allow us to directly measure the mass interchange rates between the different ISM phases defined in Section 4 in a dynamically more realistic situation. In the following, we analyse the mass exchange rates predicted by the three simulations with the different supernova locations to determine the dominant transitions between phases.

The transition rates between the different ISM phases for the simulations with random, mixed and peak driving are shown in Fig. 5 as function of time t. We express the transition rates as time derivatives of the particle fractions, $\dot{X}$, and of the dust surface

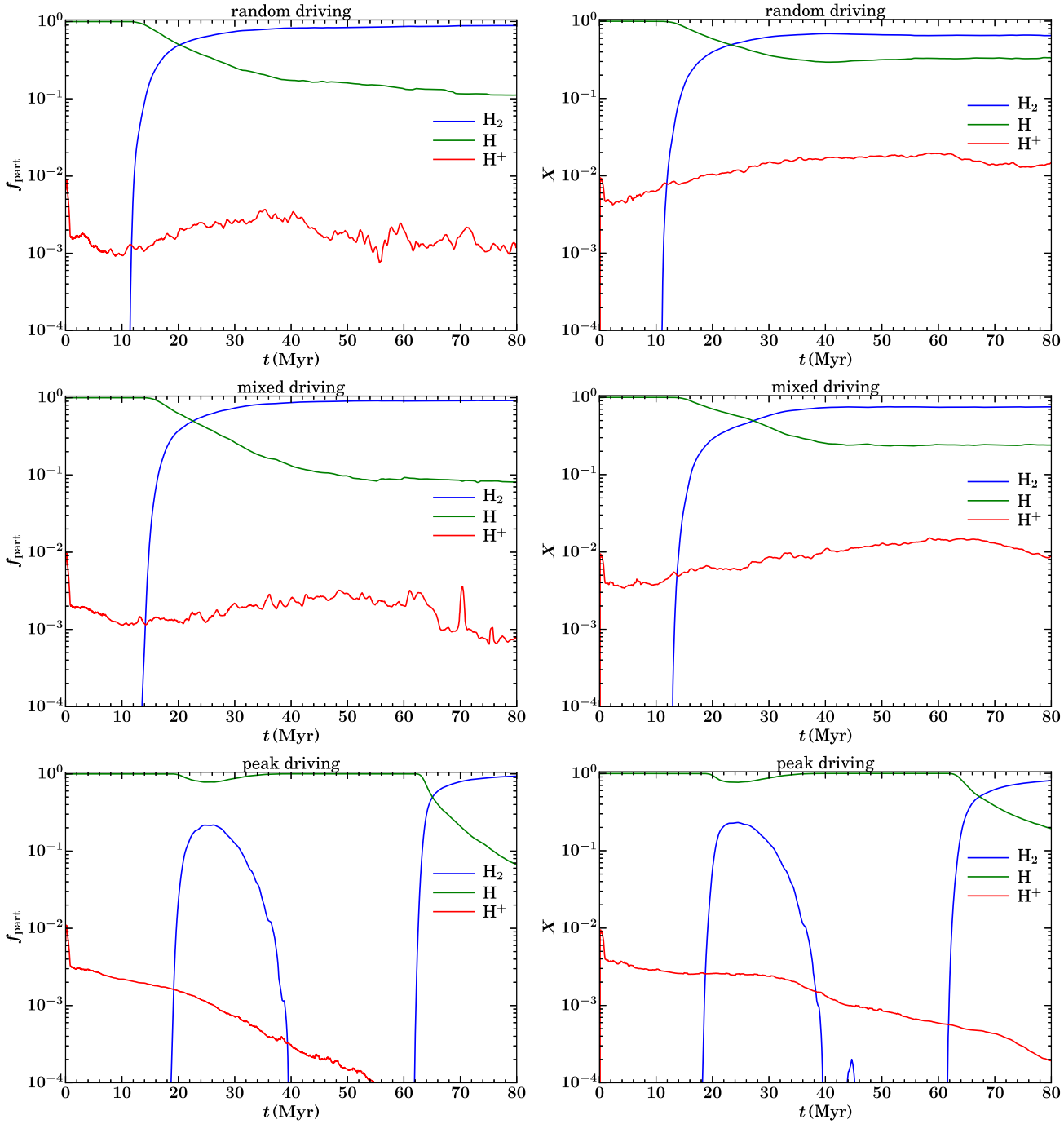

Figure 4. Particle fractions $f_{\rm part}$ (left) and total gas mass fractions X (right) for the different ISM phases defined by chemical abundances as function of time t for random (top), mixed (middle) and peak (bottom) driving.

density, $\dot{\Sigma}_{\rm d}$. Let $\dot{N}_{i\rightarrow j}(t)$ denote the number of particles transitioning from phase i to phase j at time t, then the corresponding transition rate of the particle fraction is

$$\dot{X}_{i\rightarrow j}(t) = \frac{\dot{N}_{i\rightarrow j}(t)}{N_{\rm part}}, \tag{5}$$

and the transition rate for the surface density is

$$\dot{\Sigma}_{\rm d}(t) = \frac{m_{\rm part}\dot{N}_{i\rightarrow j}(t)}{A_{\rm box}} \tag{6}$$

with the surface area of our simulation box $A_{\rm box} = (0.5\,{\rm kpc})^2$. As already noted in Section 5, it takes 10 Myr for the molecular phase to form, which is also reflected in the transition rates. After this initial period, all four ISM phases coexist in the simulations, with the exception of the disappearance of the hot phase in the peak driving run after 60 Myr.

A common feature of all transition rates is their high intermittency. The main reason for this is the sudden heating of the gas by supernova explosions and the subsequent cooling process. Depending on the location of the supernova explosion (i.e. the local

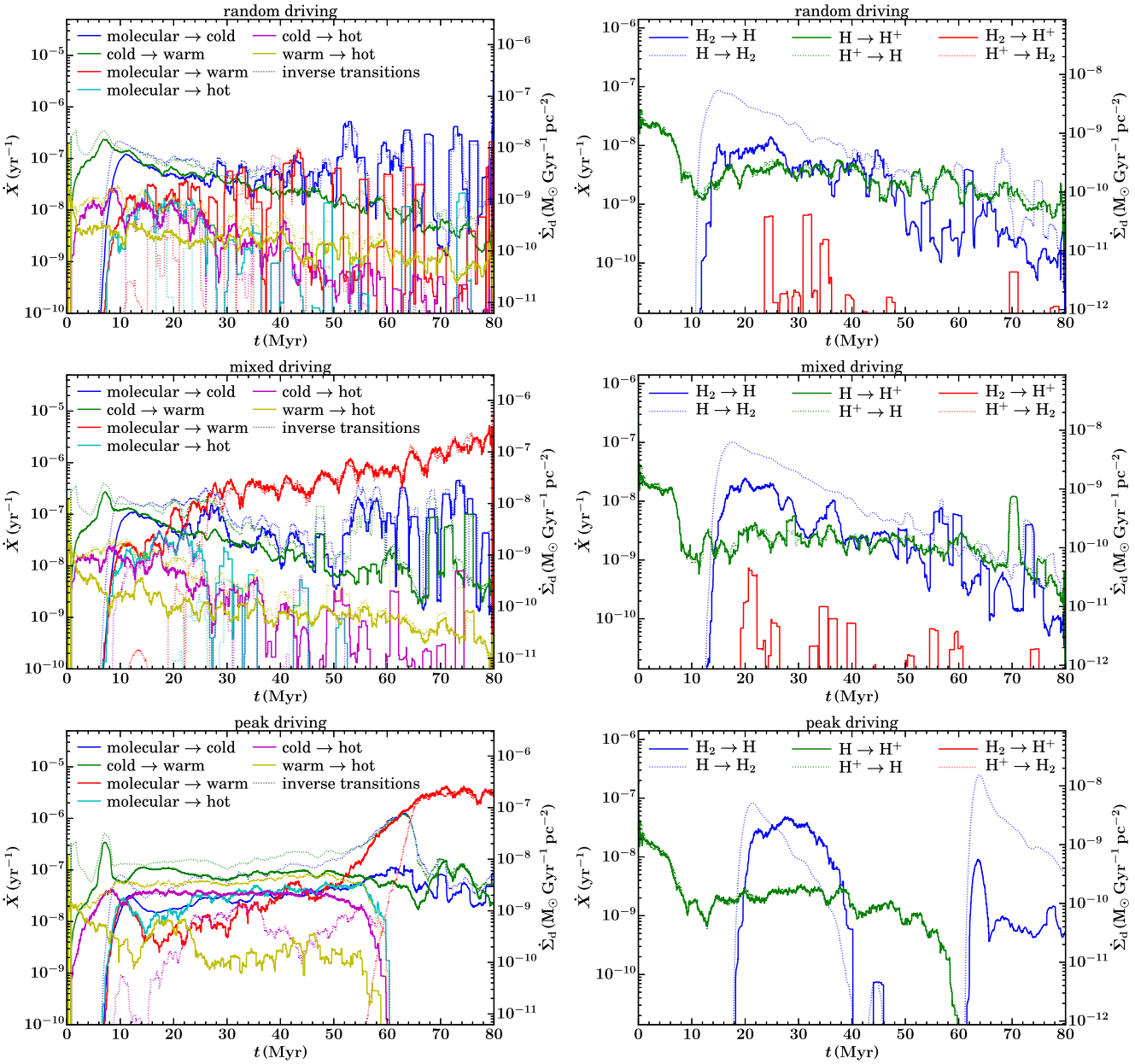

Figure 5. Transition rates of particles moving between different ISM phases defined by temperature cuts (left) and chemical abundances (right) as function of time t for random (top), mixed (middle) and peak (bottom) driving. Transitions from a cooler to a warmer phase are drawn with solid lines, and the corresponding inverse transitions from the warmer to the cooler phase with dashed lines. The ordinate on the left shows $\dot{X}$ and the right ordinate $\dot{\Sigma}_\mathrm{d}$.

gas density), both the peak temperature reached during an explosion event and the time-scale for cooling of the remnant afterwards varies. Therefore, the dominant phase transitions and their rates depend on the supernova positioning and are different for each simulation.

The simulation with random driving is dominated by the transitions between the molecular and the cold phase. This is reasonable since these two phases are directly connected and contain most tracer particles. The rate itself varies by more than an order of magnitude around a mean value of $\dot{X} \sim 10^{-7}\,\mathrm{yr}^{-1}$ or $\dot{\Sigma}_\mathrm{d} \sim 10^{-8}\,\mathrm{M}_\odot\,\mathrm{Gyr}^{-1}\,\mathrm{pc}^{-2}$. The next most dominant rate, which is roughly one order of magnitude lower, is the one between the cold and the warm phase, which again can be understood in terms of the particle fractions. These two transitions are to a very good approximation in detailed balance, meaning that the number of particles undergoing the transition from the cooler to the warmer phase equals the number of particles making the transition in the other direction. Intermittently, the direct transition from the molecular to the warm phase becomes important, too. This is an example for a transition rate in which an intermediate phase (the cold phase) is skipped at the time resolution of our sampling rate for the tracer particle data, which is 10 kyr. This effect is caused by the supernovae that explode in dense gas. The supernova injection then quickly heats up the gas and brings it into the warm phase. Usually, the cooling time after the supernova injection is much longer than 10 kyr, which explains why the inverse transition does not occur very often. Instead, cooling proceeds via the cold phase as an intermediate step.

The simulation with mixed driving shows a slightly different behaviour. Here, the transition rate between the molecular and the cold phase is comparable to the case of random driving, but the transitions between the molecular and the warm phase are now dominant. This effect is caused by the 50 per cent of all supernovae that explode at density peaks in this run. These density peaks are usually found in the molecular phase. A supernova explosion then triggers a transition into the warm phase, but at the density peaks the cooling time is short enough that tracer particles directly fall back into the molecular phase (e.g. Walch & Naab 2015; Haid et al. 2016). A small fraction of these particles does make a transition via the cold phase as an intermediate step, but the molecular and the warm phase are to a good approximation in detailed balance, as are all transitions between neighbouring phases.

The peak driving simulation shows yet another behaviour. Here, because of the suppression of the molecular phase, the molecular-cold transition is insignificant. Instead, the direct transition cold-warm and its inverse transition warm-cold are dominant. After the molecular phase has formed, the indirect transition molecular-warm and the inverse transition cold-molecular also become significant since many particles reside in the dense gas. These transitions reflect the heating and cooling cycle after supernova explosions. The injection of thermal energy brings the gas from the cold into the warm or hot phase. In the hot phase, the gas cools via the warm phase down to the cold phase again. After 60 Myr, the hot phase cannot be maintained anymore, and the supernova explosions only produce a warm phase since they explode in high-density environments and cool quickly.

The transition rates for the ISM phases defined by chemical abundances behave differently from the phases defined by temperature cuts. Here, detailed balance only occurs between the H phase and the H^+ phase. The chemical evolution for random and mixed driving is almost identical, despite the large differences in the temperature evolution. Both simulations show a significantly larger transition from the H phase into the H_2 phase than vice versa, which reflects the net H_2 formation observed in the simulations (compare Fig. 4). The transition rates for the peak driving run reveal the formation and destruction of H_2 between 20 and 40 Myr, and the disappearance of the H^+ phase and the final formation of an H_2 phase after 60 Myr.

6.1 Comparison with existing mass exchange schemes

In the following, we compare the mass transfer rates directly measured in our simulations with the rates required by simple dust evolution models to reproduce the observed differences in interstellar element depletion observed in the cold and warm medium. Draine (1990) adopts a three-phase ISM with characteristic temperatures of 30, 100 and 6000 K in the molecular, cold and warm phase, respectively. He considers two schemes for the mass circulation presented in his table III, Model A and Model B, which only differ in their mass exchange rates but otherwise have identical parameters. Model A has a molecular-cold transition rate of $1.5 \times 10^{-7}\,\mathrm{yr}^{-1}$ and a cold-warm transition rate of $8 \times 10^{-9}\,\mathrm{yr}^{-1}$. Both transitions are assumed to be in detailed balance. This model is broadly consistent with the time-averaged behaviour we see in our simulation with random driving. In contrast, his Model B assumes a molecular-cold transition rate of $3 \times 10^{-8}\,\mathrm{yr}^{-1}$ and an inverse transition rate of $2 \times 10^{-8}\,\mathrm{yr}^{-1}$. The cold-warm transition rate in this model is assumed to be $8 \times 10^{-9}\,\mathrm{yr}^{-1}$, and the inverse transition goes directly from the warm to the molecular phase with the same rate. This model is not consistent with any of our simulations, for several reasons. The magnitude of his molecular-cold transition is too small, the relative strengths of the molecular-cold and cold-warm transitions do not match, and it is difficult to get a warm-molecular transition rate that is of similar strength as the cold-warm transition rate.

Weingartner & Draine (1999) adopt a different scheme of the mass exchange in the ISM, in which molecular clouds are formed from the CNM and, upon destruction, are circulated directly to the warm phase. The CNM is formed by cooling of the WNM and can exchange mass with both the WNM and molecular clouds. Transitions from molecular clouds to the CNM or from the WNM to the molecular phase are not considered in the model. Their model includes dust growth by accretion, dust destruction in the ISM and input from stellar sources or galactic inflows. The main feature of this model is that it incorporates the enhanced accretion rates due to focusing of ions on small negatively charged grains in the cold and warm phases (see the following subsection). The transition rates between phases are then computed from the model parameters and are given in their table 3.

Their scheme of mass exchange is also not supported by our results as we observe intense mass transfer from the warm to the molecular phase in the simulations with mixed driving and from the molecular to the cold phase in the case of random driving, which are absent in Weingartner & Draine (1999). The transition rates included in their scheme of the order of a few $10^{-8}\,\mathrm{yr}^{-1}$ are roughly similar to the values predicted by our simulations, except the last 20 Myr for the mixed and peak driving simulations, when the dominant mass exchange rates exceed $10^{-7}\,\mathrm{yr}^{-1}$.

Since relative dust abundances are higher in molecular clouds, the pathway of circulation of matter from molecular clouds to warm gas influences the distribution of interstellar element depletion (O'Donnell & Mathis 1997). If dust-rich gas from molecular clouds rapidly circulates to the WNM, the average element abundances in dust in the WNM will be higher compared to the case when dust-rich matter circulates from molecular clouds to the WNM through the CNM. The latter scenario agrees with our simulation with random driving. The faster, direct circulation between molecular clouds and the warm medium appears in the simulation with mixed driving.

6.2 Model predictions for element depletion

For random and mixed driving, we study the implications of our measured transition rates for predictions of element depletion on dust grains with the simple model of Weingartner & Draine (1999). They used the observed depletion to infer the transition rates between the phases in their mass transfer scheme. Here, we reverse the procedure and take the transition rates as given to compute the depletion. For consistency, we leave all other parameters of the model unchanged. We adopt Model A and Model B of Weingartner & Draine (1999), which use different grain size distributions and destruction time-scales. Below we briefly describe the models and refer to the original publication for more details. We then compare our results with the observed depletion in the warm and cold medium. Since the transition rates in the simulations are highly fluctuating, we take the average transition rates from $t = 50$ Myr to $t = 70$ Myr. Fig. 6 shows the two mass-exchange schemes and the measured rates.

The depletion $\delta(\mathrm{X})$ of element X is defined as its gas-phase abundance relative to a reference abundance, for which we take its abundance in the Sun,

$$\delta(\mathrm{X}) = \left(\frac{n_\mathrm{X}}{n_\mathrm{H}}\right)_\mathrm{gas} \Big/ \left(\frac{n_\mathrm{X}}{n_\mathrm{H}}\right)_\odot . \tag{7}$$

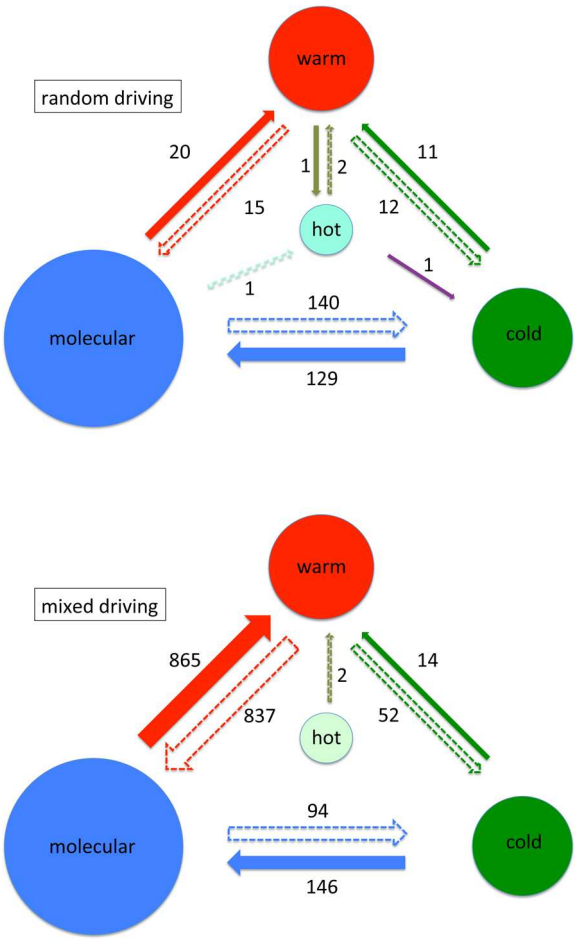

Figure 6. Schemes illustrating the dominant phase transitions (in units of 10^{-9} yr^{-1}) in the simulation with random (top) and mixed (bottom) driving averaged around $t = 60 \pm 10$ Myr. Transitions involving the hot phase are neglected in the depletion models. The sizes of the arrows indicate the strength of the transitions, and the extent of the circles illustrates the corresponding mass fractions.

Here, $n_{\rm H}$ and $n_{\rm X}$ are the number densities of hydrogen and element X, respectively. The main constituents of interstellar dust are the 'big 5' elements: Si, Mg, Fe, O and C. However, the evolution of less abundant, but more depleted elements such as Ti has been considered in the literature, because their very high depletion levels (only 5 per cent of Ti remains in the gas in the warm and less than 0.1 per cent in the cold diffuse medium) represent a more challenging problem to explain with dust evolution models (O'Donnell & Mathis 1997; Weingartner & Draine 1999).

6.2.1 *Simple steady-state model for Ti depletion*

Weingartner & Draine (1999) assume a steady state of the Ti depletion distribution between the phases to derive the mass exchange rates for the observed Ti depletion. We reverse this procedure to compute the Ti depletion δ_j in the molecular, cold and warm phase (j = m, c, w) for our measured mass exchange rates by solving the equations

$$f_j \frac{1-\delta_j}{\tau_{{\rm d},j}} + \sum_{k \neq j} \dot{X}_{k\rightarrow j}(\delta_k - \delta_j) + \frac{q_j}{f_j}\frac{1}{\tau_{\rm in}}(\delta_{\rm in} - \delta_j) = \frac{\delta_j}{\tau_{{\rm a},j}}, \qquad (8)$$

where f_j is the mass fraction of the phase j. The first term denotes the release of Ti into the gas phase due to dust destruction on the time-scale $\tau_{{\rm d},j}$. The second term is the contribution from other phases, with $\dot{X}_{k\rightarrow j}$ denoting the mass exchange rate from the phase k to the phase j in units of yr^{-1}. The third term denotes the mass input from stars or infall that happens on the time-scale $\tau_{\rm in}$, with the Ti depletion $\delta_{\rm in}$ in this material and q_j the mass fraction that goes into the phase j. It is assumed that $q_{\rm m} = 0$. Finally, the term on the right-hand side denotes the decrease of the gas-phase Ti abundance due to accretion on to the grain surfaces on the time-scale $\tau_{{\rm a},j}$.

Table 1. Parameters of the dust model. Other parameters are the same for Model A and B: $\tau_{\rm a,m} = 5.6 \times 10^6$, $\tau_{\rm d,m} = 1.0 \times 10^{10}$, $\tau_{\rm in} = 1.0 \times 10^9$, $\delta_{\rm in} = 0.1$, $q_{\rm c} = 0.1$, $g_{\rm c} = 0.05$, $g_{\rm w} = 1 - g_{\rm c}$. The time-scale of destruction $\tau_{\rm d}$ is derived in this work by minimizing the error in the resulting depletion values. All time-scales are in years.

	$\tau_{\rm a,c}$	$\tau_{\rm a,w}$	$\tau_{\rm d}$	
			Random	Mixed
Model A	4.4×10^5	1.1×10^8	1.2×10^9	4.4×10^8
Model B	2.1×10^5	6.0×10^7	8.5×10^8	3.0×10^8

Since this is a steady state model, the net inflow and outflow rates for each phase j should cancel. This condition is not strictly satisfied by our schemes, as depicted in Fig. 6. However, the deviation is so small that it would imply changes on ∼100 Myr time-scales, much longer than the time interval over which the transition rates were averaged.

The time-scale $\tau_{{\rm d},j}$ of destruction of grains in the phase j is related to the time-scale $\tau_{\rm d}$ of destruction of grains in the entire ISM by $f_{\rm c}\tau_{\rm d,c}^{-1} = g_{\rm c}\tau_{\rm d}^{-1}$ and $f_{\rm w}\tau_{\rm d,w}^{-1} = (1-g_{\rm c})\tau_{\rm d}^{-1}$, where $g_{\rm c}$ is the fraction of destruction that occurs in the cold medium. Additionally, a small amount of dust is destroyed in the molecular phase on the time-scale $\tau_{\rm d,m}$.

6.2.2 *Model parameters*

We compute the Ti depletion for Model A and B (table 3 in Weingartner & Draine 1999) that differ by the size distribution of small grains and the destruction time-scale $\tau_{\rm d}$. Both models assume extensions of the MRN power law (Mathis, Rumpl & Nordsieck 1977)

$$\frac{{\rm d}n_{\rm gr}(a)}{{\rm d}a} \sim a^{-K} \qquad (9)$$

with $K = 3.5$. Weingartner & Draine (1999) extend the classical MRN distribution, which runs from $a_{\rm min} = 5$ nm to $a_{\rm max} = 0.3$ μm, down to $a_{\rm min} = 0.4$ nm. Model A retains the MRN distribution throughout the extended grain sizes, while Model B assumes a steeper power $K = 4$ for $a < 3$ nm. Due to the higher abundance of small grains, Model B has shorter time-scales of accretion in the warm and cold medium ($\tau_{\rm a,w}$ and $\tau_{\rm a,c}$, respectively). In the molecular phase, both models assume a larger $a_{\rm min} = 15$ nm.

We adopt the same values for the model parameters as in Models A and B (see Table 1). The mass fractions f_j and mass exchange rates $\dot{X}_{k\rightarrow j}$ are taken from the simulations.

We have a different approach from Weingartner & Draine (1999) to the choice of the time-scale of destruction $\tau_{\rm d}$. Weingartner & Draine (1999) adopt the values of $\tau_{\rm d}$ at the centre of the allowed range determined by the inequalities for the transfer time-scales given by their equations (18) and (19). In our case, the transfer time-scales are input parameters determined by the numerical simulations (see Section 6.3). We compute $\tau_{\rm d}$ by optimization of the solution for $\delta_{\rm w}$ and $\delta_{\rm c}$ to provide the best fit to the observed values discussed in the next section. The resulting values for Model A are 1.2×10^9 yr

Table 2. Comparison of the predicted Ti depletion $\log \delta_j$ for mass exchange rates from the simulations with random and mixed driving with observations.

Phase	Observed $\log \delta_j$		Random driving		Mixed driving	
			Model A	Model B	Model A	Model B
Warm	-1.3^a	-1.3^b	-1.6	-1.4	-1.9	-1.8
Cold	-3.0^a	-2.9^b	-2.7	-2.9	-2.4	-2.5
Molecular	–	–	-2.6	-2.6	-2.0	-1.9

Note. [a]Values measured along the line of sight towards ζ Oph (Savage & Sembach 1996).
[b]Values for the warm and cold medium derived from the data of Jenkins (2009), see explanation in the text.

and 4.4×10^8 yr for the exchange rates from the simulations with random and mixed driving, respectively. Model B, with faster dust growth by accretion, yields somewhat lower destruction time-scales of 8.5×10^8 and 3.0×10^8 yr, respectively. The smallest standard deviation of 0.13 dex is obtained for Model B with mass exchange rates from the simulation with random driving. Generally, we find a weak dependence of the depletion on the choice of $\tau_{\rm d}$.

The values of the destruction time-scale $\tau_{\rm d}$ derived in this work are not very different from other values considered in the literature. For example, the time-scale of destruction adopted in Weingartner & Draine (1999) is 6.3×10^8 yr for Model A and 1.4×10^9 yr for Model B, respectively. Using numerical simulations of the grain evolution in interstellar shocks, Jones et al. (1996) derive a time-scale of destruction of 4×10^8 and 6×10^8 yr for silicate and carbonaceous grains, respectively. Recent revision of these values by Slavin et al. (2015) with account of uncertainties in the observed supernova rate and gas mass suggests longer values of 2–3 Gyr. Zhukovska et al. (2016) found that a lower value of 350 Myr is required in the three-dimensional dust evolution models to explain the observed Si depletion trend with the gas density.

As discussed above, the mass exchange scheme inferred from our simulations includes additional transitions in the mass exchange model compared to that of Weingartner & Draine (1999): from warm to molecular and from molecular to cold. For simplicity, we neglect the mass exchange with the hot phase, given its small mass fraction, and consider the mass exchange in the three-phase idealized ISM model.

6.2.3 *Comparison with observations*

Table 2 compares the Ti depletion values derived for the mass exchange rates from the simulations with random and mixed driving with those from observations. It is common to use the logarithmic depletion $\log \delta(\mathrm{X}) = \left[\frac{\mathrm{X_{gas}}}{\mathrm{H}}\right]$ instead of the linear depletion $\delta(\mathrm{X})$. For the warm medium, we adopt the value $\log \delta_{\rm w}(\mathrm{Ti}) = -1.3$ measured in a warm diffuse cloud along the line of sight towards ζ Oph and, for the cold medium, the value $\log \delta_{\rm c}(\mathrm{Ti}) = -3$ measured in a cold diffuse cloud along the same line of sight (Savage & Sembach 1996). Jenkins (2009) collected observational data for a large number of elements and lines of sight which represent different physical conditions. Each line of sight is characterized by the parameter F_*, which measures the overall depletion level and varies from 0 to 1 for a given data sample. Assuming $F_* = 0.12$ and $F_* = 0.90$ for the warm and cold medium, respectively (see appendix C in Jenkins 2009, for more details), we derive $\log \delta_{\rm w}(\mathrm{Ti}) = -1.3$ and $\log \delta_{\rm c}(\mathrm{Ti}) = -2.92$. Alternatively, we can apply a relation between $\log \delta_{\rm c}(\mathrm{Ti})$ and the gas volume density,

$$\log \delta_{\rm c}(\mathrm{Ti}) = \left[\frac{\mathrm{Ti_{gas}}}{\mathrm{H}}\right] = -0.895 \log n(\mathrm{H}) - 0.714, \qquad (10)$$

Table 3. Transfer time-scales and mass fractions for the mass exchange models based on random and mixed driving. Transfer time-scales $t_{i\to f} = f_i / \dot{X}_{i\to f}$ and mass fractions f_i for the mass exchange models based on the simulations with random and mixed driving from Section 6.2. Initial phases have superscript 'i' and final phases superscript 'f'. The upper (lower) values are for random (mixed) driving. All time-scales are in Myr.

	Molecular^f	Cold^f	Warm^f	Mass fraction
Molecular^i	–	5.72	39.1	0.8
	–	8.47	0.92	0.8
Cold^i	0.78	–	9.44	0.1
	0.69	–	7.00	0.1
Warm^i	6.73	8.36	–	0.1
	0.12	1.89	–	0.1

derived by combining the relation between $\log \delta_{\rm c}(\mathrm{Si})$ and the gas number density of hydrogen $n(\mathrm{H})$ given by equation 20 in Zhukovska et al. (2016) and equation 10 in Jenkins (2009), with element depletion parameters for Ti and Si taken from table 4 in Jenkins (2009). The relation is derived for the observed density range $1.2 < \log n(\mathrm{H}) < 2.8$. For the density of the CNM of 100 cm^{-3}, the relation yields a somewhat higher value $\log \delta_{\rm c}(\mathrm{Ti}) = -2.5$. There are no measurements of the gas-phase abundances of Ti in the molecular phase. Extrapolation of the relation given by equation (10) for the average density in molecular clouds of 10^3 cm^{-3} results in $\log \delta_{\rm c}(\mathrm{Ti}) = -3.4$. The estimates based on data from Jenkins (2009) are given in Table 2 for comparison.

We find a larger dependence on the mass exchange scheme than on the grain size distribution. The standard deviation in $\log \delta$ is smaller in models with mass exchange rates from the random driving scheme, with Model B providing the best fit to observations (Table 2). The effect of the enhanced accretion in the cold phase causes low values of $\log \delta_{\rm c}$ that are close to the observed values with the exchange rates from both simulations. However, in the simulation with mixed driving, Ti is too depleted in the warm phase. Because of the efficient mixing between the molecular and the warm medium in this simulation, the derived value of $\delta_{\rm m}$ is actually higher than $\delta_{\rm c}$ and is similar to $\delta_{\rm w}$, in contrast to the trend with density established for the diffuse ISM (equation 10). The mass exchange scheme from the simulation with random driving yields values of $\log \delta_{\rm w}$ which are closer to the observed ones, -1.6 and -1.4 for Models A and B, respectively. Thus, the simple model of element depletion on grains implemented here favours the mass exchange scheme from the simulation with a random positioning of supernovae.

The dispersion of the observed depletion data is modelled in Zhukovska et al. (2016). To address the origin of the scatter in the depletion consistently, we would need to implement a complete model of dust evolution, similar to the model presented by Zhukovska et al. (2016). But because of the higher spatial resolution of our simulations, we cannot immediately apply this model, as it requires a new, more accurate implementation of the destruction process.

6.3 Transfer time-scales

The two mass exchange models derived from the simulations with random and mixed driving can be further compared with simplified models such as Weingartner & Draine (1999). The transition rate $\dot{X}_{i\to f}$ between initial phase i and final phase f and the mass fraction f_i in phase i can be used to define a transfer time-scale $t_{i\to f} = f_i / \dot{X}_{i\to f}$. Table 3 shows the transfer time-scales for the two models derived from Fig. 6 (without the hot phase).

Notably, the time-scale $t_{m\rightarrow w}$ is larger than 10 Myr in all the Weingartner & Draine (1999) models, whereas for mixed driving $t_{m\rightarrow w}$ is smaller than 1 Myr. The transition time-scale $t_{c\rightarrow m}$ is also less than 1 Myr for both simulations, whereas this time-scale always exceeds 10 Myr in Weingartner & Draine (1999). The other time-scales, so far as they are present in Table 3 and Weingartner & Draine (1999), agree within a factor of a few.

7 RESIDENCE TIMES

An important quantity for understanding the processing of dust in the ISM is its residence time in the different ISM phases. In our simulations, we can directly measure these residence times from the tracer particle histories. In general, each tracer particle resides in more than one phase during the simulation runtime. In the beginning of the simulations, the ISM structure and hence the residence times are affected by our initial conditions. Near the end of the simulations, the residence times are artificially short because of the finite simulation runtime. We therefore consider the residence times for particles in a snapshot in the middle of the simulation, at $t = 40$ Myr. We have checked that we do not obtain significantly different results at $t = 30$ Myr or at $t = 50$ Myr.

At $t = 40$ Myr, we determine the current ISM phase for all tracer particles. For each particle, we then go back in time and determine at which point the particle entered this phase, and go forward to determine when it will leave the phase again. The total duration then gives the residence time for the particle in its current phase. Both the backward and the forward residence times are limited to 40 Myr, so that we cannot measure total residence times longer than 80 Myr. Some of the distributions extend all the way up to this maximum, and in these cases we would likely measure even larger residence times if we ran the simulations for longer. Likewise, we are unable to measure residence times shorter than our sampling period of 10 kyr.

Histograms of the residence time distributions are shown in Fig. 7 and cumulative probability distribution functions in Fig. 8. We list the mean and median residence times in Table 4. For random driving, the mean residence time in the molecular phase is 18 Myr. Half of the particles have a residence time less than 15 Myr, and 90 per cent of all particles have a residence time less than 34 Myr. Above 40 Myr, the frequency drops markedly. This is likely a result of the finite simulation runtime, since the molecular phase needs some time to build up. Nevertheless, the average residence time in the molecular phase is much smaller and thus unaffected by this. The cold phase has a very short average residence time of only a few Myr, with a mean (median) value of 8 (5) Myr. The longest residence times are found for the warm phase, with a mean (median) value of 36 (44) Myr. These are the particles between the clouds and in the outflow, where the dynamical times are long. Once the particles are in the warm phase, they rarely transition to the hot phase, but the dominant escape route is to the cold or molecular phase (compare Fig. 5). These routes are only available for particles within the disc, not for the majority of particles that are within the outflow. The jump at 40 Myr in the warm phase distribution comes from the fact that this is the initial phase of all particles, so we see the particles that have not left this phase yet at the time of our measurement. In contrast, particles with shorter residence times than 40 Myr must have entered the warm phase after the start of the simulation. The particles in the hot phase have a mean (median) residence time of 9 (2) Myr. The very short median is the result of supernova explosions, which transfer particles into the hot phase, but when the remnant cools down, they leave the hot phase again. The long tail of residence times comes from particles in the higher disc layers.

The residence time distributions for mixed driving are similar to the case of random driving. For peak driving, in contrast, the distributions are very different. At the time of the residence time measurement, $t = 40$ Myr, only 10 per cent of all particles are in the molecular phase (compare Fig. 3). This molecular gas is efficiently destroyed by supernova explosions at density peaks, resulting in very short residence times of only a few Myr. The hot phase is almost completely dominated by particles within the higher disc layers. As discussed previously, for peak driving supernova injections transfer particles to the warm phase, which explains the enhanced frequency of short residence times in the warm phase compared to the cases of random and mixed driving. This leads to a much reduced mean (median) value of 17 (12) Myr. The cold phase contains the majority of particles. They condense out of the warm phase, but because of the peak driving cannot settle into the molecular phase. Interestingly, the mean and median values of the residence time distribution are nevertheless very similar to the case of random and mixed driving, although the ISM is very different. We see that the multiphase ISM is not appropriately characterized by single residence times in the temperature regimes.

For the phases defined by the chemical abundances, the residence times in the H_2 phase are long. For random and mixed driving, where this phase exists, they are between 55 and 60 Myr typically. The distribution jumps at 40 Myr since many particles stay in the H_2 phase until the end of the simulation at 80 Myr, so we see the particles that have entered the H_2 phase at or earlier than the time of our measurement. Here, the maximum residence time that can be measured is affected by the simulation runtime, as can be seen in the sharp cutoff at a residence time of 70 Myr. Therefore, the true residence times would likely be even higher. The residence time distribution of the H phase is relatively flat for random and mixed driving, but has peaks at 40 and 80 Myr. The former peak is produced by particles that have remained in the H phase since the beginning of the simulation, while the latter one is created by particles that enter the wind. For peak driving, the local maximum in the H phase distribution shifts from 40 to 60 Myr. This characteristic time is created by the beginning conversion of atomic into molecular hydrogen at $t = 60$ Myr (compare Figs 4 and 5). These are the particles that have resided in the H phase since the simulation started and then transition into the H_2 phase. The residence times for the H^+ phase are similar to the hot phase in all three simulations.

The average residence times are broadly consistent with the measured transition rates. For random driving, the dominant transition rates out of the molecular and cold phase are of the order of 10^{-7} yr^{-1} at $t = 40$ Myr, leading to a $\sim$10 Myr residence time. Likewise, the dominant rate out of the H_2 phase is 5×10^{-9} Myr, resulting in a $\sim$200 Myr residence time. These order of magnitude estimates explain why the chemical phases are more affected by the finite simulation runtime than the phases defined by temperature cuts.

7.1 Comparison with estimates of molecular cloud lifetimes

It seems natural to compare the residence times in the molecular and H_2 phases with theoretical estimates of molecular cloud lifetimes. Using smoothed particle hydrodynamics (SPH) simulations of isolated disc galaxies with supernova feedback, Dobbs et al. (2012) estimated that giant molecular clouds with masses above 10^5 M$_\odot$ live for at least 50 Myr before they return their material back to the

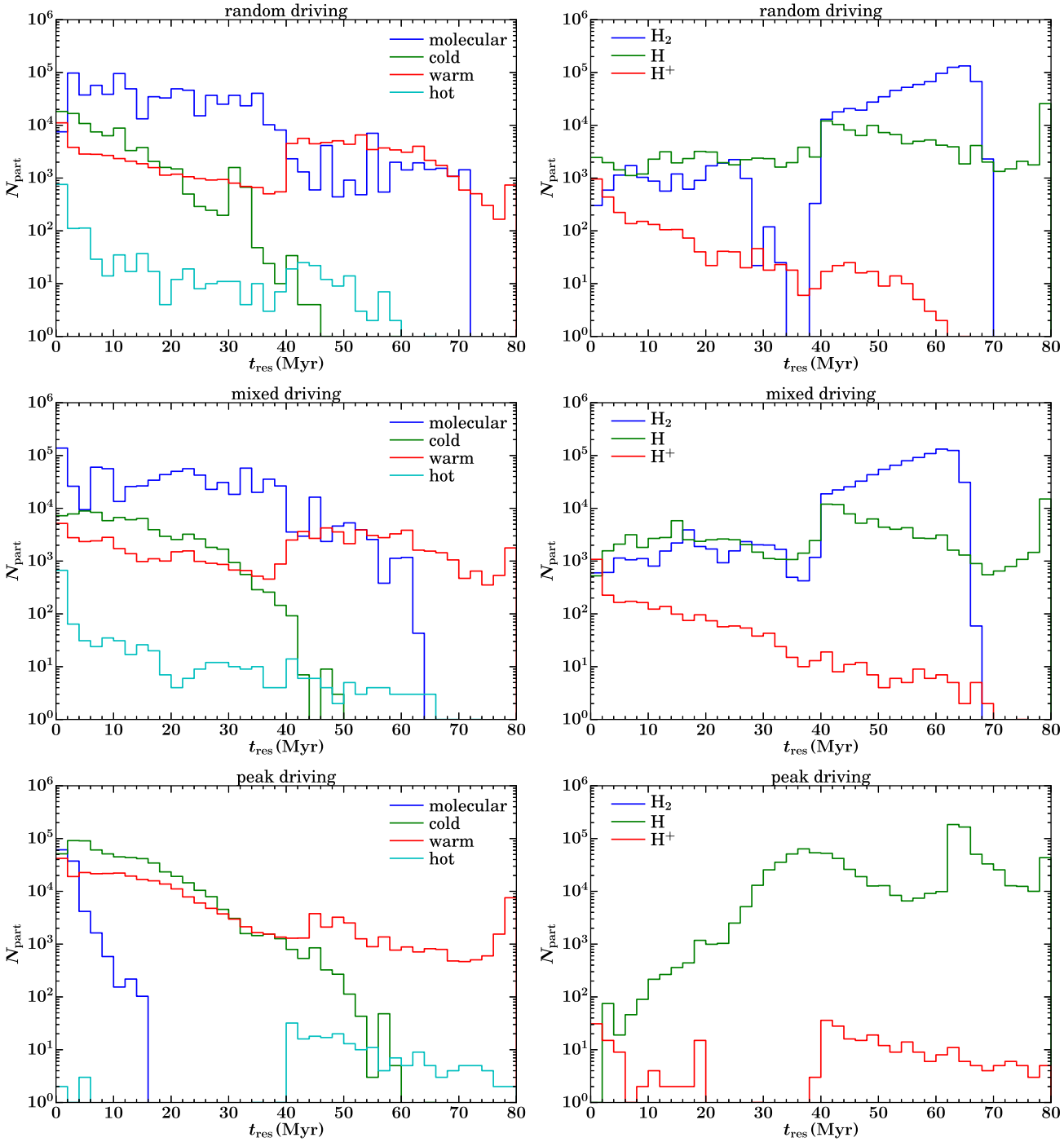

Figure 7. Histograms of the total residence time in the ISM phases defined by temperature cuts (left) and chemical abundances (right) for the particles at $t = 40$ Myr for the simulation with random (top), mixed (middle) and peak (bottom) driving.

diffuse ISM. In this work, a simple density criterion was used to decide whether an SPH particle was part of a molecular cloud or in the diffuse phase. In contrast, Dobbs & Pringle (2013), using similar simulations, employed a clump-finding algorithm to identify SPH particles belonging to giant molecular clouds and determined the cloud lifetime through the dispersal of the selected particles. This criterion led to much shorter time-scales of only 4–25 Myr for giant molecular clouds.

With a semi-analytic model of cloud destruction by photoionization feedback, Krumholz, Matzner & McKee (2006) obtained cloud lifetimes of 20–30 Myr. Our average residence times in the molecular phase are shorter, even without early stellar feedback by winds and radiation. In fact, our peak driving simulation may give better values for the molecular phase residence times in this respect than the runs with random and mixed driving, although it otherwise does not produce a realistic ISM. The small values for the molecular phase residence time are remarkable since they represent upper limits to the cloud lifetimes, given that they only measure the time spent in molecular material, during which the particles could circulate between several clouds. This is even more likely the case

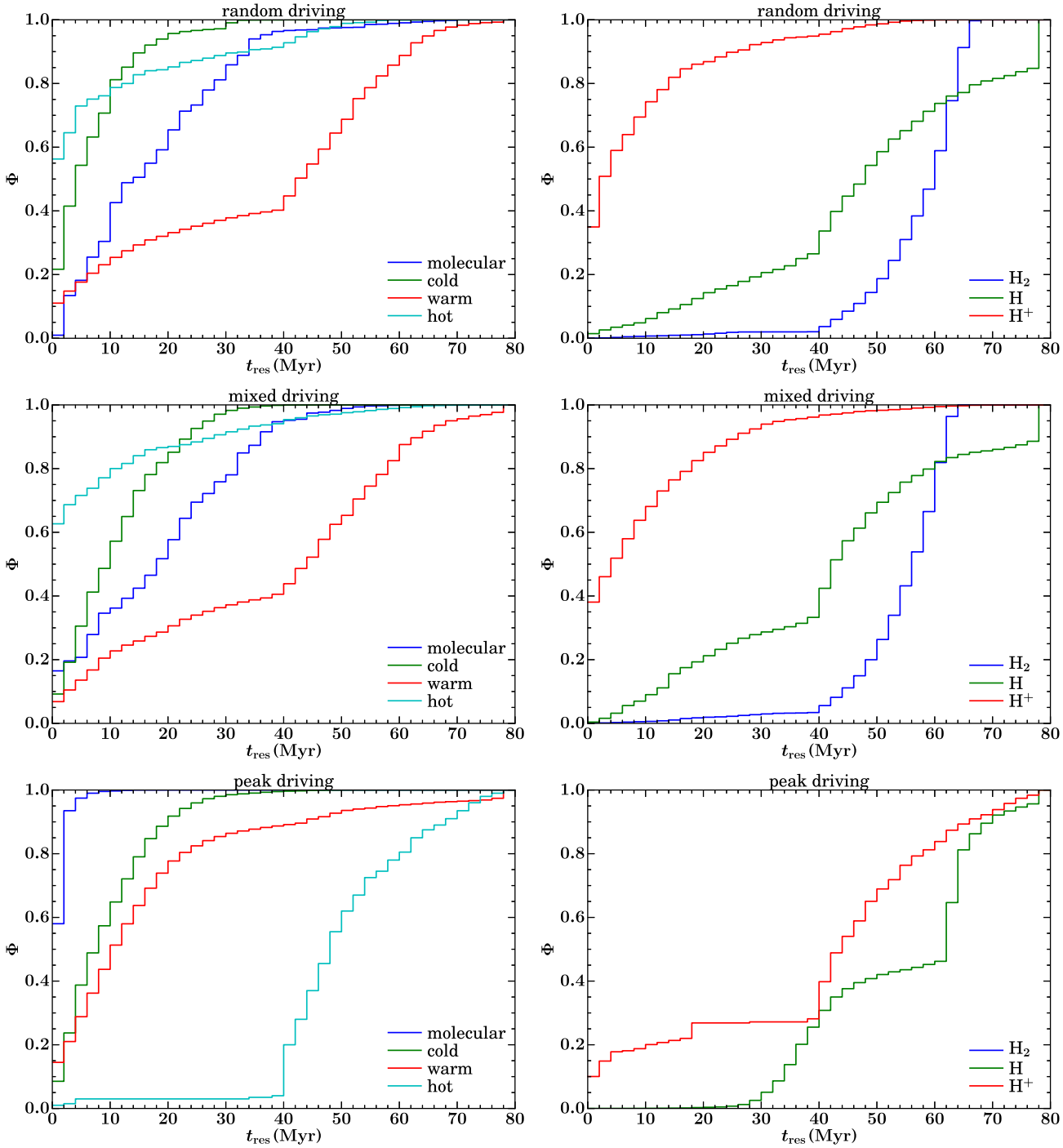

Figure 8. Cumulative probability distribution functions Φ of the total residence time in the ISM phases defined by temperature cuts (left) and chemical abundances (right) for the particles at $t = 40$ Myr for the simulation with random (top), mixed (middle) and peak (bottom) driving. The data are normalized to the total particle count per phase.

for the H_2 phase, which has much longer residence times than the molecular phase.

7.2 Implications for dust evolution models

Our study of the residence times has implications for simple models of dust evolution that treat the multiphase ISM and the mass exchange between phases in a parametrized way (Zhukovska, Gail & Trieloff 2008; Zhukovska & Gail 2009; Zhukovska 2014). In a model proposed by Zhukovska et al. (2008), the residence time of grains in molecular clouds has a fixed value and is equivalent to the lifetime of clouds $\tau_{\rm cl}$. It is an important parameter that has a two-fold effect on the rate of dust growth by accretion in the molecular clouds. If the lifetime of molecular clouds is $\gtrsim$10 times longer than the time-scale of accretion of gas-phase species on dust, which has

Table 4. Mean and median residence times in the ISM phases. Mean and median residence times of the tracer particle ensemble in the ISM phases for the three simulations at $t = 40$ Myr. The first (upper) number is the arithmetic mean, the second (lower) one is the median value of the distribution.

Supernova driving	$t_{\rm res}^{\rm mol}$ (Myr)	$t_{\rm res}^{\rm col}$ (Myr)	$t_{\rm res}^{\rm war}$ (Myr)	$t_{\rm res}^{\rm hot}$ (Myr)	$t_{\rm res}^{\rm H_2}$ (Myr)	$t_{\rm res}^{\rm H}$ (Myr)	$t_{\rm res}^{\rm H^+}$ (Myr)	$t_{\rm res}^{A_{\rm V}\leq1}$ (Myr)	$t_{\rm res}^{A_{\rm V}>1}$ (Myr)	$t_{\rm res}^{A_{\rm V}\leq3}$ (Myr)	$t_{\rm res}^{A_{\rm V}>3}$ (Myr)
Random	17.9	7.51	36.3	8.50	58.0	48.5	9.26	61.9	60.0	64.6	52.4
	15.4	5.24	43.9	1.55	60.6	48.4	3.77	67.6	61.6	79.9	54.4
Mixed	19.1	11.8	38.2	7.60	55.1	43.2	10.1	55.3	56.5	56.7	47.4
	19.3	10.3	44.6	0.765	57.3	43.8	5.40	56.2	58.2	55.4	50.4
Peak	2.06	10.2	17.0	50.6	–	54.7	40.2	50.2	11.6	68.2	–
	1.70	8.29	11.7	48.6	–	63.0	44.6	54.6	7.98	65.4	–

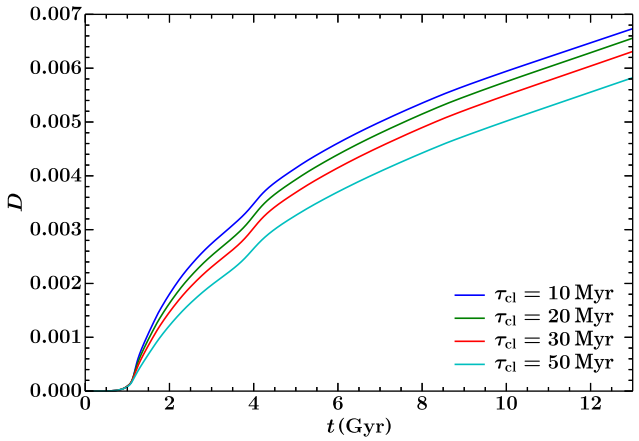

Figure 9. Evolution of the dust-to-gas ratio D in the local Milky Way for the different values of the lifetime of molecular clouds $\tau_{\rm cl} = 10$, 20, 30 and 50 Myr (from top to bottom) predicted by the model of dust evolution from Zhukovska et al. (2008).

a value of 1 Myr for the solar metallicity, then refractory elements are almost completely condensed on dust grains during their residence in molecular clouds. The matter is thus returned to the diffuse phase with the maximum dust abundances upon disruption of the clouds. However, a further increase of the cloud lifetime delays the return of the dust-rich matter to the diffuse phase and decreases the total rate of dust production in the ISM. Because the latter is the dominant mechanism of dust production in the present-day Milky Way, a longer residence time results in a lower dust-to-gas ratio.

Zhukovska et al. (2008) adopted a value of 10 Myr for the molecular cloud lifetime. It is 1.5–2 times shorter than the mean residence time in the molecular phase derived from our simulations with random and mixed driving. The distribution of the residence times is flat from a few up to 40 Myr, a large portion of grains thus reside up to four times longer than 10 Myr. A longer value of the cloud lifetime of 30 Myr has also been adopted by Tielens (1998) in his model of the dust cycle between the diffuse medium and clouds. We investigate the impact of a longer residence of grains in the molecular phase on the dust-to-gas ratio using the model of dust evolution at the local solar galactocentric radius from Zhukovska et al. (2008). Fig. 9 shows the time evolution of the average dust-to-gas ratio for different values of the $\tau_{\rm cl} = 10$, 20, 30 and 50 Myr. For the $\tau_{\rm cl} = 20$ and 30 Myr, the present dust-to-gas ratio (for $t = 13$ Gyr) is, respectively, only 3 per cent and 7 per cent lower than for the reference value. With a longer $\tau_{\rm cl} = 50$ Myr, the final dust-to-gas ratio is decreased by 15 per cent. Therefore, the broad distributions of the residence times in the molecular phase from our simulations imply a decrease in the average dust abundances by less than 10 per cent.

The derived distributions of the residence times in the ISM phases have larger consequences for the grain size and gas-phase element abundance distributions. In molecular clouds, grains grow their sizes by coagulation and accretion. Hirashita & Voshchinnikov (2014) demonstrated that, because of these processes, the residence time in the dense gas is imprinted in such observable dust characteristics as the extinction curve and element depletion. Broad distributions of the residence times in molecular clouds as found in this work imply that matter that is transferred to the diffuse phase upon disruption of clouds should exhibit large variations in the grain size and element depletion distributions. Indeed, the observed element depletion shows a large dispersion for a given gas density (Jenkins 2009). Recently, Zhukovska et al. (2016) investigated the depletion of the Si gas-phase abundance in detail with models of dust evolution in an inhomogeneous ISM. They find that the observed trend of Si depletion with density is explained by dust growth in the ISM by the accretion process, while complex histories of dust particles are responsible for the large 1 dex scatter in the observed depletion–density relation. Since accretion is a time-dependent process, the broad distributions of the residence times in the cold and molecular phases derived in this work contribute to the observed scatter in the interstellar element depletion, in addition to differences in local conditions and dynamical histories of dust particles. Similar arguments are valid for the observed variations of interstellar extinction curves (Fitzpatrick & Massa 2007).

The residence time in the warm phase determines the degree of grain processing by turbulence, which shatters large grains into smaller fragments. Our simulations with random and mixed driving yield a mean residence time in the warm medium of about 40 Myr, with a large dispersion. Longer residence times in the warm medium ($\sim$100 Myr) are required by models of the evolution of interstellar grain sizes to create a population of small grains detected by observations (Hirashita & Yan 2009; Hirashita 2010). Such a longer time-scale is necessary, because Hirashita (2010) adopt an initial size distribution dominated by large 0.1 μm grains, assuming that small grains are removed by coagulation in molecular clouds. However, as we discussed above, not all grains spend equally long times in molecular clouds (see Fig. 7), meaning that not all gas is equally processed by coagulation. Moreover, coagulation works efficiently at gas densities of 10^4 cm^{-3} and above. A large portion of molecular gas in our simulations resides at lower densities and should retain small grains.

7.3 Residence time for presolar dust grains

In addition to the processing of interstellar dust discussed above, grains are irradiated by Galactic cosmic rays. As a result, grains that remain in the ISM for a certain time have an excess of cosmic ray produced nuclides, which increases with their residence time. Some

interstellar grains that survived the formation of the Solar system can be identified in primitive meteorites. Laboratory measurements of cosmic ray produced nuclides, in particular noble gas isotopes, in these presolar grains are used to estimate the time period the grains were exposed to cosmic rays (Tang & Anders 1988; Ott et al. 2005; Heck et al. 2009). Information on the distribution of grain residence times directly measured in the laboratory provides an invaluable test for theoretical models of dust evolution.

A common assumption in this method is that the cosmic ray flux is on average constant in space. The values of the residence times in the ISM (i.e. the exposure times) derived by Heck et al. (2009) range from 3 to 1100 Myr and from 40 to 1000 Myr in work by Gyngard et al. (2009). Since the majority of the studied presolar grains have ages longer than 100 Myr, it means that they cycled a few times between the warm medium and the clouds before they got trapped during the Solar system formation. It has been shown recently that the cosmic ray ionization rate decreases in the dense molecular clouds compared to the diffuse lines of sight because low-energy cosmic rays, which are most efficient at ionization, lose their energy before they reach the interiors of dense clouds (see Indriolo & McCall 2012, and references therein). Using hydrodynamical simulations of the ISM evolution, we find that on average the grains spend two times longer in the warm gas compared to the molecular cloud (about 20 and 40 Myr, respectively), and, additionally, 5–15 Myr in the cold diffuse medium. Thus, about one-third of their residence in the ISM, grains spend at the environment with a lower ionization rate. Taking the cycle of grains in the multiphase ISM into account may lead to longer cosmic ray exposure times in the ISM inferred in presolar grain studies. This issue will be addressed using the probability distribution functions for the residence times in the dense and diffuse medium from ISM simulations including cosmic rays (Peters et al. 2015; Girichidis et al. 2016b; Simpson et al. 2016) together with different cosmic ray ionization rates in these phases in our future work.

8 SHIELDING

Dust grains undergo different processing when they are exposed to the interstellar radiation field or shielded from it. For every grid cell, we determine A_V by the arithmetic mean of 4π steradian maps of the total hydrogen column density using the `TreeCol` algorithm (Clark et al. 2012). We restrict the column density calculation to a radius of 50 pc and take the periodic boundaries in the disc plane into account (Walch et al. 2015). Since we thus know the strength of the radiation field at the location of the tracer particles, we can compute the residence times in regions of high and low A_V. We consider two different threshold values $A_{V,thresh}$, namely $A_{V,thresh} = 1$ and $A_{V,thresh} = 3$. The value $A_V = 3$–4 is the threshold extinction for the detection of ice mantles around dust grains derived in infrared spectroscopic observations (Murakawa, Tamura & Nagata 2000; Whittet et al. 2001).

We show the histograms of residence times at $t = 40$ Myr for the three simulations in Fig. 10 and the cumulative probability distribution functions in Fig. 11. We have used exactly the same procedure to produce the statistics as for the ISM phases. Just as with the previous histograms, the results for random and mixed driving are very similar. The statistics for $A_{V,thresh} = 1$ and $A_{V,thresh} = 3$ is not very different at the highest particle counts, which implies that gas at these extinctions collapses into molecular clouds and is dispersed on very similar time-scales. Qualitatively, the histograms resemble the distributions for the H_2 phase in Fig. 7 for random and mixed driving. Quantitatively, there are more particles in the

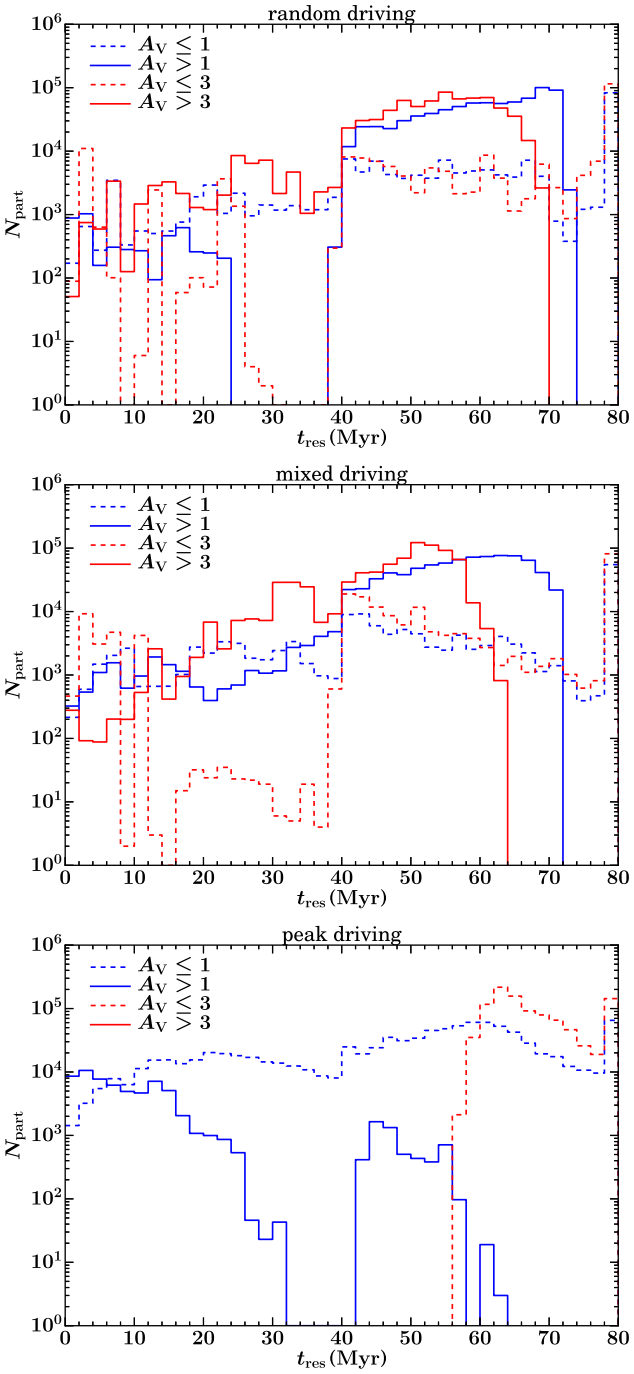

Figure 10. Histograms of total residence times at $t = 40$ Myr in regions with $A_V \leq A_{V,thresh}$ and $A_V > A_{V,thresh}$ for $A_{V,thresh} = 1$ and $A_{V,thresh} = 3$ for the simulation with random (top), mixed (middle) and peak (bottom) driving.

H_2 phase than with $A_V > 1$ since $A_V \sim 0.1$–0.2 is sufficient to form H_2 due to self-shielding. The large residence times imply that both shielding from as well as exposure to the interstellar radiation field are typically long-term processes that last more than 50 Myr, at least in the absence of early feedback. For peak driving, with the constant supernova injections in dense gas, particles with $A_V > 3$ do not exist, and most particles reside in regions with $A_V \leq 1$ for a long time. Some particles do have $A_V > 1$, although there is no H_2 phase at this time of the simulation. This again illustrates that it

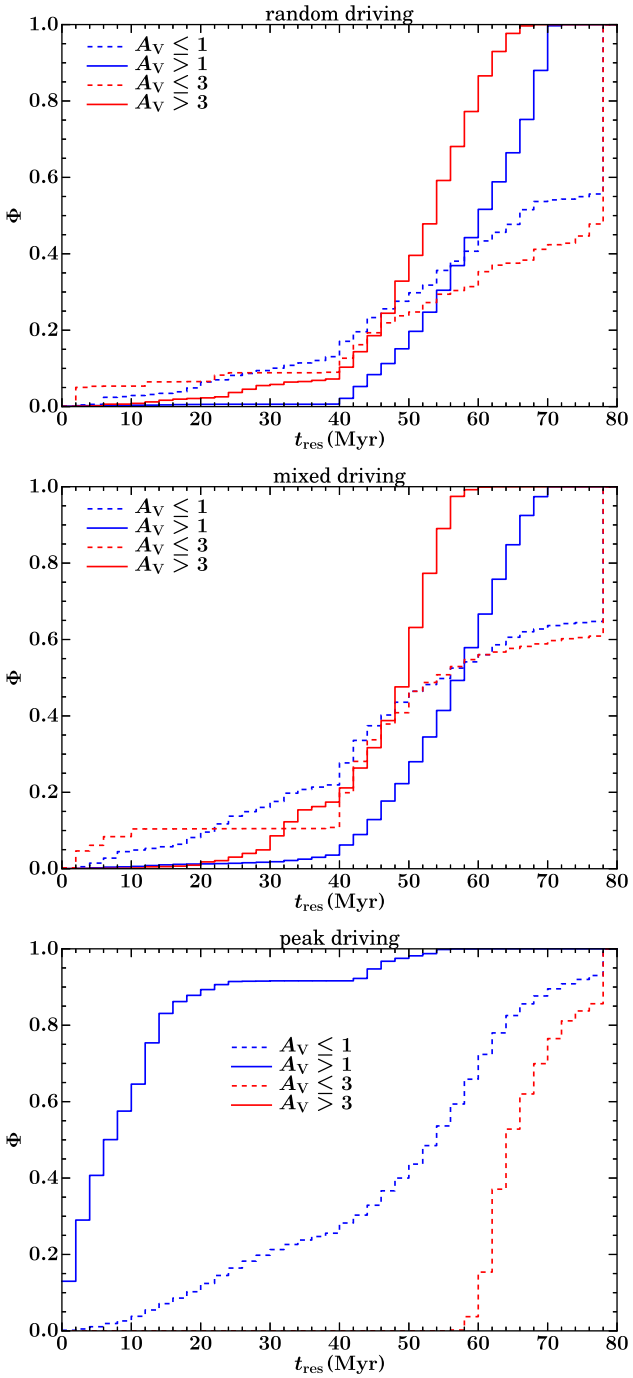

Figure 11. Cumulative probability distribution functions Φ of total residence times at $t = 40$ Myr in regions with $A_V \leq A_{V,thresh}$ and $A_V > A_{V,thresh}$ for $A_{V,thresh} = 1$ and $A_{V,thresh} = 3$ for the simulation with random (top), mixed (middle) and peak (bottom) driving. The data are normalized to the total particle count per phase.

is not possible to properly characterize the multiphase ISM with a single quantity like A_V.

9 CAVEATS

The analysis presented in this work is only a first step. Here, we aim at a systematic investigation of different methods of supernova positioning in simulations where supernovae explode at a constant rate. Clearly, some of our results will be different for more realistic simulations. Self-consistent and early feedback by stellar winds (Gatto et al. 2017) and radiation (Peters et al. 2017) will likely reduce the residence time of grains in the molecular and H_2 phase. Early feedback will also mitigate the overcooling problem for supernova explosions in dense gas by creating cavities inside clouds before the first supernovae explode (Walch & Naab 2015). This may significantly alter the transition rates. Self-consistent feedback also allows for self-regulation of star formation, so that our simulations can reach some form of steady state in the ISM properties. Our measured transition rates and residence times would then be independent of the stage of the simulation.

Further caveats are related to our simulation setup. Including galactic rotation through shearing box boundary conditions may contribute to cloud disruption and further reduce the molecular and H_2 residence times. Furthermore, our limited numerical resolution in the dense gas may also affect our measured residence times in the molecular and H_2 phase and in regions with $A_V > 3$. Finally, the non-uniform sampling of the ISM by the Lagrangian tracer particles leads to discrepancies between gas mass fractions and particle fractions. This disagreement should be eliminated to better represent the simulated ISM with the tracer particle technique. We plan to address these issues in future work.

10 CONCLUSIONS

We present a pilot study in which we measure, for the first time, the residence times of interstellar dust in the different ISM phases, and the transition rates between the phases. We use hydrodynamical simulations from the SILCC project that are similar to previous work (Walch et al. 2015; Girichidis et al. 2016a), but with a smaller box height and with Lagrangian tracer particles to probe the physical conditions for interstellar dust grains. We find complex evolutionary histories of the dust grains, which in general reside in multiple ISM phases during the simulation runtime. The development of the ISM phases, the dominant transition rates between phases and the residence times are a strong function of supernova positioning, that is they differ depending on whether supernovae explode at random positions, at density peaks or as a mixture of the two.

In simulations with random and mixed driving, the resulting ISM is similar. For random driving, transitions between the molecular and cold phase dominate, followed by transitions between the cold and warm and intermittently between the molecular and warm phases. For mixed driving, molecular-warm transitions outweigh the other transitions because of the 50 per cent fraction of peak supernovae. Most of the transitions are in detailed balance. For peak driving, the formation of a molecular phase is suppressed initially, and the hot phase eventually disappears. Hence, the transition rates change significantly at different stages of the simulation. For the most realistic simulations with random and mixed driving, we model the Ti gas-phase depletion with a simple model of dust evolution using the measured transition rates. We find the best agreement with observations in the warm and cold phases for random driving.

Residence times generally have broad distributions, in contrast to the single values used in idealized models. The residence time distribution in the runs with random and mixed driving is similar, with median residence times in the molecular, cold, warm and hot phase around 17, 7, 44 and 1 Myr, respectively. Peak driving, in contrast, leads to median residence times of 2, 8, 12 and 49 Myr in these phases. The residence times in the cold phase agree well in all simulations, although the ISM structure is very different. Therefore, single residence times are not a good description of the multiphase

ISM. The broad distribution of residence times in the molecular phase implies a reduction of the dust-to-gas ratio at the percent level in the dust and chemical evolution model by Zhukovska et al. (2008), and may contribute to the scatter in the observed gas-phase element depletion.

ISM phases defined by chemical abundance rather than temperature cuts are more stable with respect to perturbations by shocks and supernova explosions. They therefore generally show smaller transition rates and have longer residence times. For random and mixed driving, the median residence times in the H_2 and H phase are around 59 and 45 Myr, respectively. The residence time in H_2-dominated gas is therefore significantly longer than the residence time in gas with $T \leq 50$ K, which stresses the importance of including chemistry in simulations of the multiphase ISM. In contrast, the residence time distribution in the H^+ phase coincides with the hot phase distribution. The A_V residence time statistics agree well with the statistics for the H_2 phase.

Our results indicate the great potential of hydrodynamical simulations of the multiphase ISM to provide detailed information on variable physical conditions for interstellar grains. They can further the development of more physical models of the dust life cycle in the ISM. Future investigations with a more self-consistent and complete treatment of star formation and stellar feedback as well as simulations over longer time intervals will overcome some of our current limitations.

ACKNOWLEDGEMENTS

We thank Fabian Heitsch and Edward Jenkins for helpful discussions and the referee for helpful comments that improved the clarity of the paper. All simulations have been performed on the Odin and Hydra clusters hosted by the Max Planck Computing & Data Facility (http://www.mpcdf.mpg.de/). TP, ZS, TN, PG, SW, SCOG and RSK acknowledge the *Deutsche Forschungsgemeinschaft* (*DFG*) for funding through the SPP 1573 'The Physics of the Interstellar Medium'. TN acknowledges support by the DFG cluster of excellence 'Origin and structure of the Universe'. SW acknowledges funding by the Bonn-Cologne-Graduate School, by SFB 956 'The conditions and impact of star formation', and from the European Research Council under the European Community's Framework Programme FP8 via the ERC Starting Grant RADFEEDBACK (project number 679852). SCOG and RSK acknowledge support from the DFG via SFB 881 'The Milky Way System' (sub-projects B1, B2 and B8). RSK acknowledges support from the European Research Council under the European Community's Seventh Framework Programme (FP7/2007-2013) via the ERC Advanced Grant STARLIGHT (project number 339177). The software used in this work was developed in part by the DOE NNSA ASC- and DOE Office of Science ASCR-supported Flash Center for Computational Science at the University of Chicago. The data analysis was partially carried out with the YT software (Turk et al. 2011).

REFERENCES

Amari S., Zinner E., Gallino R., 2014, Geochim. Cosmochim. Acta, 133, 479
Bakes E. L. O., Tielens A. G. G. M., 1994, ApJ, 427, 822
Barnes J., Hut P., 1986, Nature, 324, 446
Bekki K., 2015, MNRAS, 449, 1625
Bergin E. A., Tafalla M., 2007, ARA&A, 45, 339
Bouchut F., Klingenberg C., Waagan K., 2007, Numer. Math., 108, 7
Caselli P., 2011, in Cernicharo J., Bachiller R., eds, Proc. IAU Symp. 280, The Molecular Universe. Cambridge Univ. Press, Cambridge, p. 19
Clark P. C., Glover S. C. O., Klessen R. S., 2012, MNRAS, 420, 745
Dobbs C. L., Pringle J. E., 2013, MNRAS, 432, 653
Dobbs C. L., Pringle J. E., Burkert A., 2012, MNRAS, 425, 2157
Draine B. T., 1990, in Blitz L., ed., ASP Conf. Ser., Vol. 12, The Evolution of the Interstellar Medium. Astron. Soc. Pac., San Francisco, p. 193
Draine B. T., 2009, in Henning T., Grün E., Steinacker A., eds, ASP Conf. Ser. Vol. 414, Cosmic Dust - Near And Far. Astron. Soc Pac., San Francisco, p. 453
Draine B. T., 2011, Physics of the Interstellar and Intergalactic Medium. Princeton Univ. Press, Princeton, NJ
Draine B., Li A., 2007, ApJ, 657, 810
Dubey A., Antypas K., Ganapathy M. K., Reid L. B., Riley K., Sheeler D., Siegel A., Weide K., 2009, Parallel Comput., 35, 512
Ferrière K. M., 2001, Rev. Mod. Phys., 73, 1031
Fitzpatrick E. L., Massa D., 2007, ApJ, 663, 320
Fontani F., Giannetti A., Beltrán M. T., Dodson R., Rioja M., Brand J., Caselli P., Cesaroni R., 2012, MNRAS, 423, 2342
Fryxell B. et al., 2000, ApJS, 131, 273
Gatto A. et al., 2015, MNRAS, 449, 1057
Gatto A. et al., 2017, MNRAS, 466, 1903
Genel S., Vogelsberger M., Nelson D., Sijacki D., Springel V., Hernquist L., 2013, MNRAS, 435, 1426
Girichidis P. et al., 2016a, MNRAS, 456, 3432
Girichidis P. et al., 2016b, ApJ, 816, L19
Glover S. C. O., Clark P. C., 2012, MNRAS, 421, 116
Glover S. C. O., Mac Low M.-M., 2007a, ApJS, 169, 239
Glover S. C. O., Mac Low M.-M., 2007b, ApJ, 659, 1317
Glover S. C. O., Smith R. J., 2016, MNRAS, 462, 3011
Glover S. C. O., Federrath C., Mac Low M.-M., Klessen R. S., 2010, MNRAS, 404, 2
Gnat O., Ferland G. J., 2012, ApJS, 199, 20
Goldsmith P. F., 2001, ApJ, 557, 736
Goldsmith P. F., Langer W. D., 1978, ApJ, 222, 881
Greenberg J. M., 1982, in Clube S. V. M., McInnes B., eds, Comets. Univ. Arizona Press, Tucson, AZ, p. 131
Gyngard F., Amari S., Zinner E., Ott U., 2009, ApJ, 694, 359
Haid S., Walch S., Naab T., Seifried D., Mackey J., Gatto A., 2016, MNRAS, 460, 2962
Heck P. R. et al., 2009, ApJ, 698, 1155
Hirashita H., 2000, ApJ, 531, 693
Hirashita H., 2010, MNRAS, 407, L49
Hirashita H., Voshchinnikov N. V., 2014, MNRAS, 437, 1636
Hirashita H., Yan H., 2009, MNRAS, 394, 1061
Hocuk S., Cazaux S., Spaans M., 2014, MNRAS, 438, L56
Hollenbach D., Kaufman M. J., Bergin E. A., Melnick G. J., 2009, ApJ, 690, 1497
Indriolo N., McCall B. J., 2012, ApJ, 745, 91
Jenkins E. B., 2009, ApJ, 700, 1299
Jenniskens P., Baratta G. A., Kouchi A., de Groot M. S., Greenberg J. M., Strazzulla G., 1993, A&A, 273, 583
Jones A. P., Tielens A. G. G. M., Hollenbach D. J., McKee C. F., 1994, ApJ, 433, 797
Jones A., Tielens A., Hollenbach D., 1996, ApJ, 469, 740
Jones A. P., Fanciullo L., Köhler M., Verstraete L., Guillet V., Bocchio M., Ysard N., 2013, A&A, 558, A62
Kennicutt R. C. Jr., 1998, ApJ, 498, 541
Krumholz M. R., Matzner C. D., McKee C. F., 2006, ApJ, 653, 361
McKee C., 1989, in Allamandola L. J., Tielens A. G. G. M., eds, Proc. 135th Symp. IAU, Interstellar Dust. Kluwer, Dordrecht p. 431
McKee C. F., Ostriker J. P., 1977, ApJ, 218, 148
McKinnon R., Torrey P., Vogelsberger M., 2016, MNRAS, 457, 3775
Martin P. G. et al., 2012, ApJ, 751, 28
Mathis J. S., Rumpl W., Nordsieck K. H., 1977, ApJ, 217, 425
Murakawa K., Tamura M., Nagata T., 2000, ApJS, 128, 603
Nelson R. P., Langer W. D., 1997, ApJ, 482, 796
O'Donnell J. E., Mathis J. S., 1997, ApJ, 479, 806

Ormel C. W., Min M., Tielens A. G. G. M., Dominik C., Paszun D., 2011, A&A, 532, A43
Ott U., Altmaier M., Herpers U., Kuhnhenn J., Merchel S., Michel R., Mohapatra R. K., 2005, Meteorit. Planet. Sci., 40, 1635
Peters T. et al., 2015, ApJ, 813, L27
Peters T. et al., 2017, MNRAS, 466, 3293
Planck Collaboration XXIV, 2011, A&A, 536, A24
Planck Collaboration XI, 2014, A&A, 571, A11
Planck Collaboration XVII, 2014, A&A, 566, A55
Rachford B. L. et al., 2009, ApJS, 180, 125
Roman-Duval J. et al., 2014, ApJ, 797, 86
Roy A. et al., 2013, ApJ, 763, 55
Savage B. D., Sembach K. R., 1996, ARA&A, 34, 279
Schmidt M., 1959, ApJ, 129, 243
Simpson C. M., Pakmor R., Marinacci F., Pfrommer C., Springel V., Glover S. C. O., Clark P. C., Smith R. J., 2016, ApJ, 827, L29
Slavin J. D., Dwek E., Jones A. P., 2015, ApJ, 803, 7
Soifer B. T., Sanders D. B., Madore B. F., Neugebauer G., Danielson G. E., Elias J. H., Lonsdale C. J., Rice W. L., 1987, ApJ, 320, 238
Tammann G. A., Löffler W., Schröder A., 1994, ApJS, 92, 487
Tang M., Anders E., 1988, ApJ, 335, L31
Tielens A. G. G. M., 1998, ApJ, 499, 267
Tielens A. G. G. M., 2010, The Physics and Chemistry of the Interstellar Medium. Cambridge Univ. Press, Cambridge
Tielens A., McKee C., Seab C., Hollenbach D., 1994, ApJ, 431, 321
Turk M. J., Smith B. D., Oishi J. S., Skory S., Skillman S. W., Abel T., Norman M. L., 2011, ApJS, 192, 9
Waagan K., 2009, J. Comput. Phys., 228, 8609
Waagan K., Federrath C., Klingenberg C., 2011, J. Comput. Phys., 230, 3331
Walch S., Naab T., 2015, MNRAS, 451, 2757
Walch S. et al., 2015, MNRAS, 454, 238
Weingartner J., Draine B., 1999, ApJ, 517, 292
Whittet D. C. B., Gerakines P. A., Hough J. H., Shenoy S. S., 2001, ApJ, 547, 872
Wolfire M. G., Hollenbach D., McKee C. F., Tielens A. G. G. M., Bakes E. L. O., 1995, ApJ, 443, 152
Wooden D. H., Charnley S. B., Ehrenfreund P., 2004, Comets II, 33
Zhukovska S., 2014, A&A, 562, A76
Zhukovska S., Gail H.-P., 2009, in Henning T., Grün E., Steinacker J., eds, ASP Conf. Ser., Vol. 414, Cosmic Dust - Near and Far. Astron. Soc. Pac., San Francisco, p. 199
Zhukovska S., Gail H.-P., Trieloff M., 2008, A&A, 479, 453
Zhukovska S., Dobbs C., Jenkins E. B., Klessen R., 2016, ApJ, 831, 147
Zubko V., Dwek E., Arendt R. G., 2004, ApJS, 152, 211

This paper has been typeset from a TEX/LATEX file prepared by the author.